



THESIS APPROVAL

GRADUATE SCHOOL, KASETSART UNIVERSITY

Doctor of Engineering (Mechanical Engineering)

DEGREE

Mechanical Engineering

Mechanical Engineering

FIELD

DEPARTMENT

TITLE: Mixed Numerical-Experimental Technique for Identification of Constitutive Parameters

NAME: Mr. Rittipol Chantararat

THIS THESIS HAS BEEN ACCEPTED BY

THESIS ADVISOR

(Mr. Prapot Kunthong, Ph.D.)

THESIS CO-ADVISOR

(Assistant Professor Wichai Siwakosit, Ph.D.)

THESIS CO-ADVISOR

(Mrs. Anchana Wongsto, Ph.D.)

DEPARTMENT HEAD

(Associate Professor Chawalit Kittichaikarn, Ph.D.)

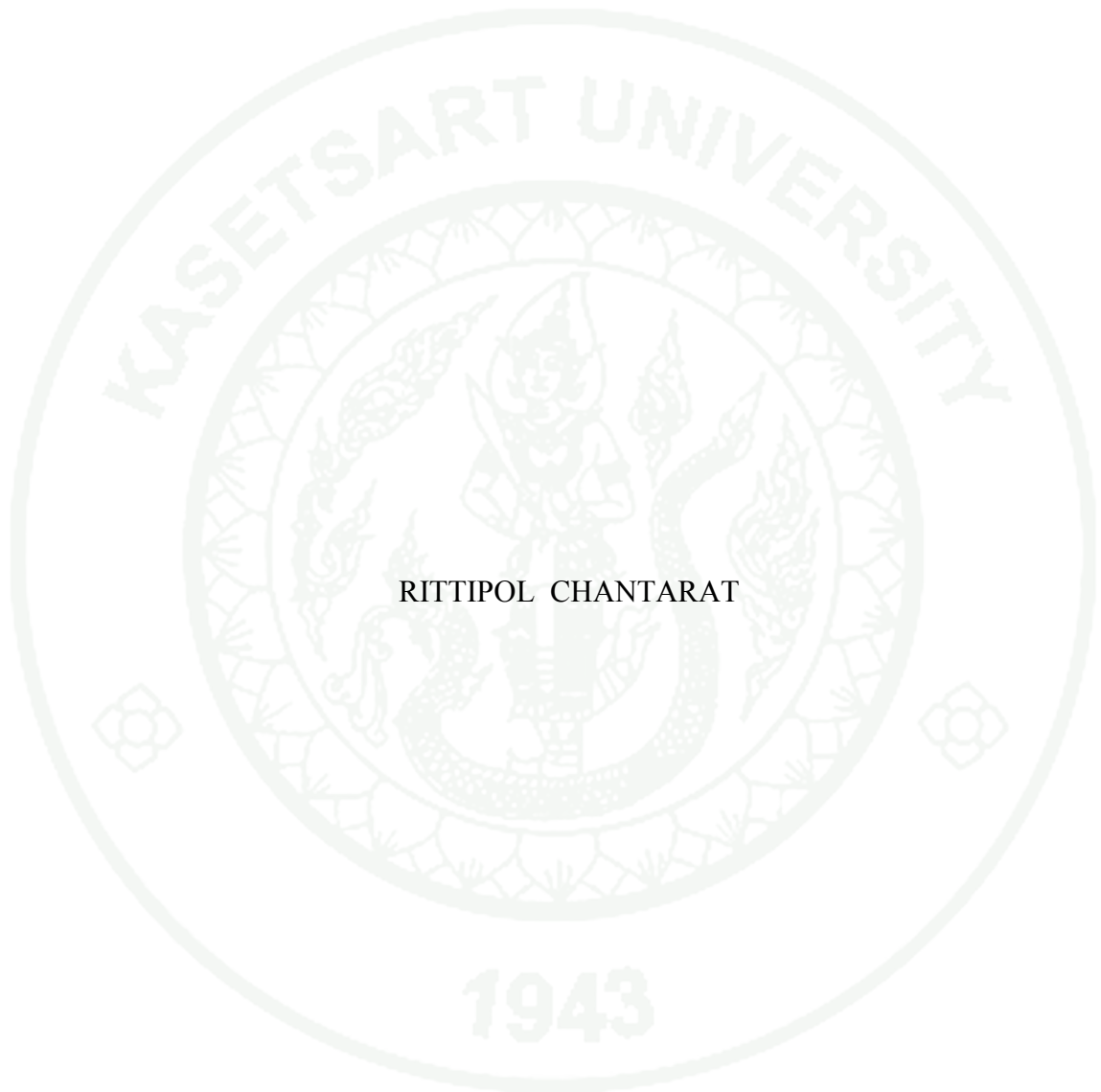
APPROVED BY THE GRADUATE SCHOOL ON _____

DEAN

(Associate Professor Gunjana Theeragool, D.Agr.)

THESIS

MIXED NUMERICAL-EXPERIMENTAL TECHNIQUE FOR
IDENTIFICATION OF CONSTITUTIVE PARAMETERS



RITTIPOL CHANTARAT

A Thesis Submitted in Partial Fulfillment of
the Requirements for the Degree of
Doctor of Engineering (Mechanical Engineering)
Graduate School, Kasetsart University

2013

Rittipol Chantarat 2013: Mixed Numerical-Experimental Technique for Identification of Constitutive Parameters. Doctor of Engineering (Mechanical Engineering), Major Field: Mechanical Engineering, Department of Mechanical Engineering. Thesis Advisor: Mr. Prapot Kunthong, Ph.D. 86 pages.

Full-field measurement of deformations using digital image correlation, DIC, technique is investigated in this work. The technique yields the surface deformation by correlating a pair of digital images, one before loading, and the other after loading. The DIC algorithms including sub-pixel methods were studied and implemented for analyzing the displacement fields. The experiment on deformation of cantilever beam was performed to demonstrate the DIC measurement.

The analytical solution of an infinite plate with a circular hole is introduced for investigating algorithm errors in identification of material parameters instead of performing actual experiments. The simulated speckle image pairs, consisting of undeformed images and deformed images, are created from analytical function. Then, a new formulation of DIC based on optical flow and finite element methods is developed to estimate heterogeneous displacement fields from simulated speckle images. The compliance coefficients of testing materials are iteratively computed by mixed numerical-experimental technique (MNET). The isotropic and orthotropic models of material parameters are investigated for accuracy of the purposed algorithms. The interaction between algorithm errors is studied. The sources of errors are discussed and progressive improvement is suggested for these identification techniques. Finally, discontinuous finite element method is applied to conservation of optical flow to circumvent discontinuous problems.

Student's signature

Thesis Advisor's signature

ACKNOWLEDGEMENTS

This thesis would not have been possible unless the kindness of advisor team. Foremost, I would like to express sincere gratitude to my thesis advisor, Prof. Prapot Kunthong for his patience, guidance, enthusiasm and immense knowledge. Beside my advisor, I would like to thank my co-advisor: Asst. Prof. Wichai Siwakosit and Prof. Anchana Wongsto, for insightful comments and suggestions. I thank my fellow labmates and friends in Kasetsart University for helps and stimulating discussion. Last but not for the least, I would like to thank my family: my parents Vinia Chantararat and Niramom Chantararat, my wife Witchuda Chantararat, for supporting me spiritually throughout my life.

Rittipol Chantararat

February 2013

TABLE OF CONTENTS

	Page
TABLE OF CONTENTS	i
LIST OF TABLES	ii
LIST OF FIGURES	iii
LIST OF ABBREVIATIONS	iv
INTRODUCTION	1
OBJECTIVES	4
LITERATURE REVIEW	5
MATERIALS AND METHODS	10
RESULTS AND DISCUSSIONS	35
CONCLUSIONS AND RECOMMENDATIONS	48
LITERATURE CITED	50
APPENDICES	55
Appendix A MATLAB codes using in study of DIC algorithms	56
Appendix B MATLAB codes for MNET	63
CURRICULUM VITAE	86

LIST OF TABLES

Table		Page
1	Comparison of theory displacements and measured displacements	38
2	Relative errors in L_2 -norm of U and V displacements on ZOI	39
3	Elastic coefficients using isotropic model	42
4	Elastic coefficients using orthotropic model	43

LIST OF FIGURES

Figure		Page
1	2D-DIC equipment arrangement	10
2	Searching for the best matching between undeformed and deformed subsets	12
3	Mapping functions from undeformed and deformed subsets	15
4	Experimental setup of the cantilever beam measured by DIC	18
5	Flow-chart of MNET for identify material parameters	19
6	An infinite plate with a central hole	20
7	Synthetic pattern of an undeformed image and histogram of gray levels on an undeformed image	21
8	ZOI domain Ω consisting of many element domains and one elemental domain Ω^e consisting of many subsets Ω^{sn} of spline functions	25
9	FEM mesh and FEM boundary condition and ZOI	27
10	Computing DIC strains from Q4 elements and triangular elements	30
11	Separation movement of two objects and their displacements	34
12	Synthetic speckle patterns	35
13	Percentage errors of DIC measurements	36
14	Deformation of cantilever beam	37
15	DIC x-y analytical displacement (a), (b) and x-y DIC displacement (c), (d) on ZOI	40
16	Analytical strains (a), (c), (e) and FEM strains (b), (d), (f)	41
17	Measured displacements of optical flow based on continuous and discontinuous finite element method	46
18	Absolute displacement errors of optical flow based on continuous finite element and discontinuous finite element	47

LIST OF ABBREVIATIONS

DIC	=	Digital image correlation
MNET	=	Mixed numerical-experimental technique
C	=	Cross-correlation coefficients
f	=	Grey value of undeformed images or subsets
g	=	Grey value of deformed images
f_m	=	Average of grey value in undeformed images or subsets
g_m	=	Average of grey value in deformed images or subsets
u	=	Displacements in x-direction
v	=	Displacements in y-direction
U	=	Displacements in x-direction
V	=	Displacements in y-direction
a_{mn}	=	Spline coefficients of undeformed subsets
b_{mn}	=	Spline coefficients of deformed subsets
Δ	=	Delta denoted the change of any variable quantity
∇	=	Gradient operators
$\nabla \cdot$	=	Divergence operators
$\nabla \nabla$	=	Second order gradients
$\underline{s}, s_{11}, s_{12}, s_{22}, s_{66}$	=	Compliance coefficients
E	=	Young's modulus
ν	=	Poisson's ratio
d	=	displacement
\mathbf{W}	=	Weighting martrix
$b(x,y)$	=	Image noise

MIXED NUMERICAL-EXPERIMENTAL TECHNIQUE FOR IDENTIFICATION OF CONSTITUTIVE PARAMETERS

INTRODUCTION

Developing mathematical models for stress analyses is cumbersome in design phases. In conceptual designs, the analysts make assumptions to define geometries, materials, loads and so on. The finite element method (FEM) is a simple way to analyze mathematical models. However, when the components or prototypes exist, situations involving real components are partially specified. After all, the analysts can not be completely aware of every material properties, every aspect of the loading, and every condition of environment for these particular components. The unknown parameters which can not identify by only analytical procedures lead designers to do trials and errors of experimental and analytical methods. The experiments are used to measure some unknowns, and guesses/assumptions are used to fill in remaining unknowns (Doyle, 2004).

An *inverse* problem is one where we know something of the responses (usually by measurement) and wish to infer something of the systems or the inputs. For examples, the measurements of loads (inputs) and strains (responses) on a uniaxial specimen infer the Young's modulus (systems). In fact, all experimental problems can be thought of as inverse problems because we begin with response information and wish to infer something about the systems or unknowns (Doyle, 2004). The assumptions such as boundary conditions, material properties, loads, and dimensions in finite element methods make the results of the analyses uncertain and unreliable. The most direct way of narrowing the unreliability in the results is to simply measure the unknown. In case of dimensions, it can measure directly. However, in case of Young's modulus of irregular specimen geometries and anisotropic materials, indirect measurements might be suitable to identify this parameter. How to use indirect measurements to find the solution of partially

specified problems is an important concern of this research. The finite element method is combined with experimental methods to identify unknowns or solutions.

Identifying constitutive parameters for materials is an inverse problem for mechanical design. The heterogeneous displacements as in composite materials are difficult to measure by simple strain gages. Many steps of measurements and many sampling points make analysis too slow in developments and production of composites. The accuracy and precision of measurements are the main factors that have to take into accounts. Then, the optic metrology is incorporated with inverse techniques facilitating measurements. The full-field non-contact measurements, for example, Photoelasticity (Frocht, 1941; Frocht, 1948), Moire' (Post *et al.*, 1994), Digital Image Correlation (DIC) (Sutton *et al.*, 2009) and Electronic Speckle Pattern Interferometer (ESPI) (Jacquot and Fournier, 2000), can gather tremendous full-field data for stress-strain measurements. Therefore, designers can easily apply these data through inverse techniques to identify material properties. The key point is to identify material properties by two snap-shot of camera, load and unload of specimens.

Identification of elastic properties of materials is very important for establishing constitutive equations in mechanical models. Irregular specimen geometries and anisotropic behavior of materials are not simple to identify material properties with old traditional methods. Therefore, mixed numerical-experimental technique (MNET) (Cardon *et al.*, 2004) integrated with digital image correlation (DIC) offers an alternative tool that eases material-testing methods. An advantage of MNET and DIC is to identify all material parameters in a single test with acceptable accuracy. The actual experiments are able to simulate in computers and suggestion of experimental modification can be made to improve precision and accuracy of measurements.

The errors and noises of hardware and software algorithm play an important role for accuracy and precision in the development of MNET and DIC. There are many literatures that study about errors of MNET and DIC but they study separately. The resolution of digital cameras, arrangement of all devices, lighting conditions,

lens, speckle patterns and subset sizes influence accuracy of DIC measurements (Haddadi and Belhabib, 2008). In addition, different DIC algorithms can give results in different errors (Bing *et al.*, 2006). Not only DIC algorithms but also MNET algorithms might be able to magnify systematic errors due to assumption of boundary condition, mesh configuration and finite element model construction. To quantify systematic errors of measurements, the connectivity between DIC errors and MNET errors should be addressed before doing the real experiments.

The aim of this work is to introduce computer simulation to identify elastic parameters of isotropic materials in order to reduce the length and the cost of the “trial and error” phase in experimental setup and computer program developments. The novel DIC algorithm based on optical flow and MNET are developed to identify isotropic properties of materials by using isotropic models and orthotropic models. The interconnection errors between DIC errors and MNET errors are studied and they are evaluated by analytical solution. Moreover, an advantage of computer simulation throughout identification processes can establish the baseline before doing the actual experiments. Finally, performing the real experiments confirms possibility and accuracy of the simulations.

OBJECTIVES

The overall objectives of this research shall be to identify constitutive parameters of materials by the uses of mixed numerical-experimental technique (MNET). A Full-field measurement, digital image correlation (DIC), has been developed for better suites with experiments. The final goal is to improve all algorithms for flexibility, accuracy and robust. The new numerical algorithms will be purposed for the better precision of measurements. This research will be focused on algorithm developments.

There are three major objectives will be pursued for this research.

1. Basic principles of 2D-DIC algorithms such as template matching and sub-pixel registration algorithms are studied for the concepts and implementation. The computer simulation is introduced to evaluate algorithm accuracy using simple rigid body translation and cantilever beam deflection.
2. The Q4-DIC and MNET algorithms are developed for identification of isotropic properties of a plate with a central hole. The computer simulation is introduced to facilitate experimental setup. The interconnection errors between DIC errors and MNET errors are studied and they are evaluated by analytical solution.
3. To circumvent discontinuous problems such as cracks and object separation, the conservation of optical flow based on discontinuous finite element method is formulated and tested for performance and accuracy.

LITURATURE REVIEW

The inverse methods to identify mechanical material parameters by using digital images began in developments of computer visions and numerical algorithms. The higher performances and lower prices of digital cameras are attractive to researchers in using digital images to measure displacements and strain fields instead of pointwise measurements such as strain gauges. The displacements and strain fields measured from digital images are used as inputs for inverse algorithms to determine material properties. To extract displacement fields from digital images, numerous sub-pixel algorithms of digital image correlation (DIC) are introduced to solve the problems such as least square correlation coefficient based on Newton-Raphson iteration (N-R method) and optical flow method.

In 1982, Peters and Ranson proposed digital imaging techniques to measure surface displacement fields in laser speckle metrology. The methods suggested a comparison of digital images before and after deformation using small regions (or subsets). Using this approach, Sutton *et al.* (1983) developed a numerical algorithm that is to match two speckle patterns before and after deformation by correlation scheme. Improving accuracy, Bruck *et al.* (1989) introduced a first-order Taylor series expansion for the mapping functions to capture displacement gradients. Moreover, Lu and Cary (2000) increased accuracy by a second-order Taylor series expansion for the mapping functions or shape functions. A least square correlation coefficient is used to determine the optimum values for the mapping parameters. The Newton-Raphson iteration method is used to solve systems of nonlinear equations that are calculated from minimizing the least square correlation coefficient. Then, large-deformation measurements can be achieved ± 0.0002 for the first-order displacement gradients and ± 0.0002 per pixel for the second-order displacement gradients. The DIC based on the Newton-Raphson methods was applied to determine displacement fields from STM (Scanning tunneling microscope) (Vendroux *et al.*, 1998; Vendroux and Knauss, 1998b, 1998a). The resolution yields 4.8 nm for in-plane and 1.5 nm for the out-of-plane displacement.

Even through least square correlation coefficient based on Newton-Raphson iteration has the highest accuracy than optical flow method, the computation time is longer than optical flow method (Bing *et al.*, 2006). The optical flow that is apparent motion of objects in images can arise from relative motion of objects and the viewers (Gibson, 1950). The image brightness, position and time are derived in partial derivative equations to estimate optical flow. Since optical flow is an ill-posed problem, the calculus of variation and a spatial regularization were proposed by Horn and Schunck (1981) to determine displacement fields that are based on an assumption of smooth displacements. For large motions, Lucas and Kanade (1981) developed registration techniques using optical flow and Newton-Raphson iteration. The convergences of Lucas-Kanade algorithm are studied and the range of convergences will be improved by suppressing high spatial frequencies in the images. To gain better interface between optical flow and finite element method, finite element method based on conservation of optical flow that is called Q4-DIC is developed by Besnard *et al.* (2006) to study Portevin-Le Chatelier bands in an aluminum alloy sample.

Hild and Roux (2006) using Q4-DIC measured displacements from Brazilian disk tests to identify material properties of polycarbonate disks. The closed-form solutions of displacements of Brazilian disk test are referred to the subject in elasticity. Identifying material properties, the closed-form solutions of displacements are compared with DIC measurement displacements by least square method. The noisy strains can be recovered by the so-called integrated approach. The difficulty to find the closed-form solutions for complex geometries and ambiguous boundary conditions leads to develop alternative methods such as the finite element model updating method (FEMU), the virtual fields method (VFM)(Grédiac *et al.*, 2002a, 2002b, 2003), the equilibrium gap method (EGM), the constitutive equation gap method (CEGM) and the reciprocity gap method (RGM). Avril *et al.* (2008) reviews these methods intensively in a journal article.

The FEMU or MNET is the most intuitive approach that consists in performing iteratively finite element simulations to find constitutive parameters. The iterative processes will be achieved when the best match between computed and experimental measurements satisfy acceptable relative errors. The forces and displacements are measured from the sensors and the least-square method is formed to compute searched material parameters (Pagnacco *et al.*, 2005). The alternative MNET by using resonant frequency of orthotropic metal plates is very efficient to identify orthotropic properties (Lauwagie *et al.*, 2003). The resonant frequencies of metal plates are measured by Resonalyser procedures. Then, the resonant frequencies that are related to elastic properties of materials are compared by weighted least squares. Not only identifying elastic coefficients but also other mechanical parameters such as natural frequency of structures (Sinha and Friswell, 2003) can be detected.

The use of heterogeneous or inhomogeneous strain fields gives rise for identification of material parameters due to geometry complexity of design components and anisotropic properties of materials. The heterogeneous displacement fields of a plate with a hole in uniaxial tension are measured by the ESPI methods and strains are computed from the heterogeneous displacement fields. The MNET identifies the orthotropic material parameters by comparing FEM strains and measured strain (Lecompte *et al.*, 2005). Likewise, DIC measures displacements of biaxial tests on cruciform specimens and the MNET identifies mechanical properties of glass fibre reinforced epoxy (Lecompte *et al.*, 2007). However, measuring heterogeneous strain fields by conventional DIC still requires accuracy improvement.

To improve accuracy in measuring heterogeneous strain fields, the least square method with adaptive spatial regularization was developed to determine displacements of a plate with a hole under biaxial loads and rectangular specimens with lateral slits under tensile loads (Cofaru *et al.*, 2010b). The regularized methods improve mean errors up to 50 percents smaller compared to the non-regularized methods. Most DIC algorithms are based on continuous displacement hypothesis. In contrast, discontinuous formulation of DIC using extended finite element methods

(XFEM) (Mohammadi, 2008), which is called X-DIC, is developed to capture discontinuous displacements. The X-DIC is useful for detecting localized shear band (Réthoré *et al.*, 2007), cracks (Réthoré *et al.*, 2008a) and 3D cracks (Réthoré *et al.*, 2008b).

The XFEM based on enrichment terms in field variables that are created from analytical solutions is called intrinsic enrichment (Fries and Belytschko, 2006). In addition, the enrichment terms called extrinsic enrichment can be created from set of the partition of unity functions (Babuška and Melenk, 1997). In contrast, discontinuous finite element method (DFEM) concerns the discontinuity across the element boundaries (Reed and Hill, 1973). There are various approaches of discontinuous finite element method such as interior penalty (IP) method for hyperbolic equations (Burman *et al.*, 2010). For a one-dimensional inverse problem, the discontinuous Galerkin (DG) method using a Tikhonov regularization is developed for parameter sought (Epshteyn *et al.*, 2009). For advantages of both XFEM and DG, a combination of XFEM and DG leads to XFEM-DG (Gracie *et al.*, 2008) which deals with the discontinuity in elements and the discontinuity across element boundary.

The biases or errors of DIC measurements are studied in various literatures. The greyscale interpolations such as bicubic spline and Fourier interpolation are required for sub-pixel accuracy and displacement shape function are required for improving accuracy. However, interpolation of greyscale and displacements might cause inaccuracy and interpolation biases to the DIC algorithms. The systematic errors in DIC due to undermatched subset shape functions of displacements (Schreier and Sutton, 2002) are studied for error analysis. Next, the systematic errors in DIC caused by gray-value interpolations are studied and the methods reducing these errors are proposed (Schreier *et al.*, 2000). Other parameters such as sizes of the speckles (Lecompte *et al.*, 2006), sizes of subsets and speckle patterns (Pan *et al.*, 2008) that relate to the errors of DIC measurements are identified and analyzed. Intuitive methods to quantify errors of DIC are to use synthetic images that are generated by computers. The synthetic deformed images imposed by a sinusoidal displacement

fields is utilized to quantify errors of DIC (Bornert *et al.*, 2009). The errors using deformation of Bi-axial loading of an infinite plate with a hole and realistic ground truth speckle images quantify errors of N-R methods based DIC and the gradient-based DIC methods (Cofaru *et al.*, 2010a).



MATERIALS AND METHODS

1. Study of DIC algorithms

Image matching is a discipline of computer vision that is to detect objects in motion. The 2D DIC employs concepts of image matching to detect motion of studied objects. For in-plane measurements of DIC, experimental set-up can be displayed as figure 1. The white light is emitted from the lighting sources and it is reflected from the specimen surfaces to a digital camera by passing through a camera lens. The specimen surfaces should be painted with random speckle patterns to create a unique identity for analysis regions. During loading, the specimens should be parallel to an image sensor to prevent errors from out-of-plane motions. Next, a digital camera captures the speckle pattern images of specimen surfaces before and after loading. Both speckle pattern images carry displacement information of deformed specimen surfaces waiting for computer analyses.

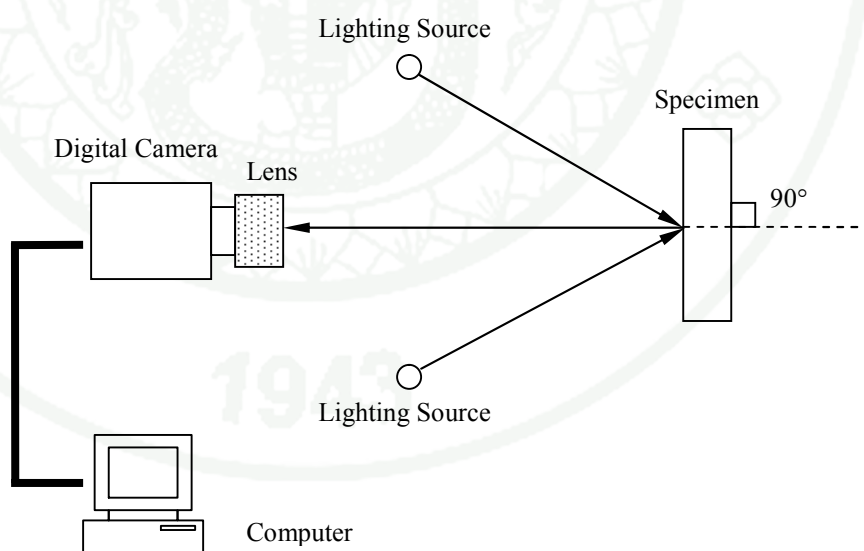


Figure 1 2D-DIC equipment arrangement.

The image sensors in digital cameras are very important for DIC accuracy. Selection of image sensors for DIC can be CCD (Charge-Couple Devices) or CMOS (Complementary Metal Oxide Semiconductor) sensor. In physics, light consider as photons. The mechanism of image sensors is to converse a number of photons that hits the pixel during exposure time to create electrons. The electrons are collected and form a charge which is transformed into voltage after the end of exposure. This voltage is amplified and digitized to gray value for each pixel. An image is represented as a 2D array of pixels and a pixel is the smallest entity in an image.

1.1 Simple search methods

For simple motion measurement, a subset of $(2i+1) \times (2j+1)$ from the undeformed image is chosen to find its location in the deformed image as figure 2. Searching the best matching between a subset of an undeformed image and a subset of an deformed image is to utilize the cross-correlation coefficients. The definition of the cross-correlation coefficients can be expressed as

$$C(u, v) = \frac{\sum_{x=-i}^i \sum_{y=-j}^j [(f(x, y) - f_m)(g(x+u, y+v) - g_m)]}{\sqrt{\left(\sum_{x=-i}^i \sum_{y=-j}^j (f(x, y) - f_m)^2 \right) \times \left(\sum_{x=-i}^i \sum_{y=-j}^j (g(x+u, y+v) - g_m)^2 \right)}} \quad (1)$$

where $f(x, y)$ and $g(x+u, y+v)$ are the grey values of each pixel in undeformed and deformed subsets. f_m and g_m are the averages of grey values in the subsets. u and v are x and y displacements of subset centers. The values of cross-correlation coefficients in eq.(1) have the ranges -1 to 1. If $|C(u, v)|$ is close to 1, undeformed subsets likely relate to deformed subsets. On the other hands, if $|C(u, v)|$ is close to 0, undeformed subsets unlikely relate to deformed subsets. The accuracy of measured displacements of this method is one pixel because the minimal unit in digital image is one pixel.

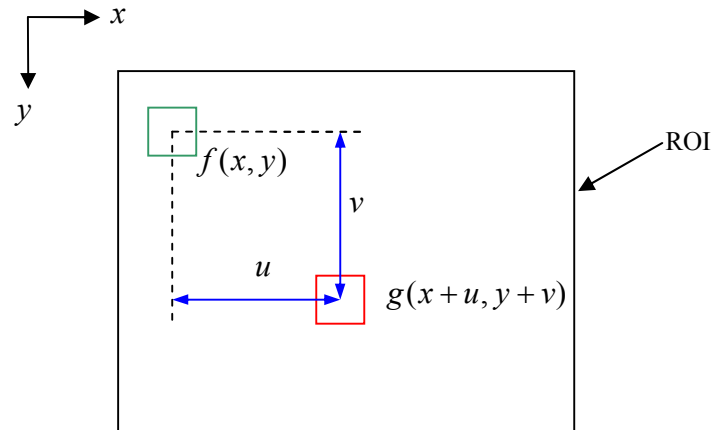


Figure 2 Searching for the best matching between undeformed and deformed subsets.

1.2 Newton-Raphson Method

Improving DIC algorithm accuracy from integer pixel resolution to sub-pixel resolution, different sub-pixel algorithms have been developed by many researchers. One type of various sub-pixel algorithms is least square methods based on Newton-Raphson iteration or N-R methods which is more accurate than other methods such as optical flow method and correlation coefficient curve-fitting method (Bing *et al.*, 2006; Hung and Voloshin, 2003). However, computational time of N-R methods is longer than other methods due to iterative computation. The development of N-R methods for sub-pixel accuracy has a need to interpolate grey values of an undeformed image $f(x, y)$ and a deformed image $g(\tilde{x}, \tilde{y})$ by using bicubic splines:

$$f(x, y) = \sum_{m=0}^3 \sum_{n=0}^3 a_{mn} x^m y^n$$

$$g(\tilde{x}, \tilde{y}) = \sum_{m=0}^3 \sum_{n=0}^3 b_{mn} \tilde{x}^m \tilde{y}^n \quad (2)$$

(x, y) is the positions of grey values at each pixel in undeformed images and (\tilde{x}, \tilde{y}) is the positions of grey values at each pixel in deformed images. a_{mn} and b_{mn} are coefficients of spline functions which are determined by using grey values and their gradients of each pixel position.

If a body is subjected to a system of forces, individual points of the body will move. This movement of an arbitrary point is a vector quantity known as a displacement. If the various points in the object undergo different movements, each can be represented by its own unique displacement vector. For two dimensions, each vector can be decomposed into components parallel to a set of Cartesian coordinate axes. For examples, u and v are the displacement components in the x and y directions, respectively.

Motion of the object can be considered as the sum of two parts (Dally and Riley, 1991), rigid-body motion and deformation. The *rigid-body motion* is the translation or rotation of the whole body and the *deformation* is the movement of the points of the body relative to each other. The rigid body motions can be large or small. Deformations, in general, are small except when rubberlike materials or specialized structure as long, slender beams are involved. DIC measures both rigid-body displacements and deformation displacements.

An advantage of N-R methods is to introduce the mapping functions or shape functions to increase DIC accuracy for approximating deformation in the subsets. First order and second order Taylor series approximation of displacement functions are introduced to create mapping functions. Figure 3 illustrates how to map subset points in an undeformed subset to a deformed subset. The center point P in the undeformed subset located at position (x_p, y_p) is moved to the center point \tilde{P} in deformed subset located at position $(x_{\tilde{p}}, y_{\tilde{p}})$. The relation of (x_p, y_p) and $(x_{\tilde{p}}, y_{\tilde{p}})$ can be expressed as

$$\begin{aligned}x_{\tilde{p}} &= x_p + U_p \\y_{\tilde{p}} &= y_p + V_p\end{aligned}\quad (3)$$

where U_p and V_p are displacement components at point P in the x and y directions respectively. First order Taylor series approximation of $U(x, y)$ and $V(x, y)$ about (x_p, y_p) is given by:

$$\begin{aligned}U(x, y) &= U(x_p, y_p) + (x - x_p) \left. \frac{\partial U}{\partial x} \right|_{x_p, y_p} + (y - y_p) \left. \frac{\partial U}{\partial y} \right|_{x_p, y_p} \\V(x, y) &= V(x_p, y_p) + (x - x_p) \left. \frac{\partial V}{\partial x} \right|_{x_p, y_p} + (y - y_p) \left. \frac{\partial V}{\partial y} \right|_{x_p, y_p}\end{aligned}\quad (4)$$

From figure (3), the point Q in the undeformed subset located at (x_Q, y_Q) is moved to the point \tilde{Q} in deformed subset located at $(x_{\tilde{Q}}, y_{\tilde{Q}})$. The point \tilde{Q} has the relation to point P as

$$\begin{aligned}x_{\tilde{Q}} &= x_p + \Delta x + U_Q \\y_{\tilde{Q}} &= y_p + \Delta y + V_Q\end{aligned}\quad (5)$$

where U_Q and V_Q are displacement components at point Q in the x and y directions. $\Delta x = (x_Q - x_p)$ and $\Delta y = (y_Q - y_p)$. Using eq.(4) to approximate U_Q and V_Q in eq.(5) rewrites eq.(5) as

$$\begin{aligned}x_{\tilde{Q}} &= x_Q + U_p + \left. \frac{\partial U}{\partial x} \right|_{x_p, y_p} \Delta x + \left. \frac{\partial U}{\partial y} \right|_{x_p, y_p} \Delta y \\y_{\tilde{Q}} &= y_Q + V_p + \left. \frac{\partial V}{\partial x} \right|_{x_p, y_p} \Delta x + \left. \frac{\partial V}{\partial y} \right|_{x_p, y_p} \Delta y\end{aligned}\quad (6)$$

Other points instead of point Q can be rewritten in general forms as

$$\begin{aligned}\tilde{x} &= x + u + \frac{\partial u}{\partial x} \Delta x + \frac{\partial u}{\partial y} \Delta y \dots\dots \\ \tilde{y} &= y + v + \frac{\partial v}{\partial x} \Delta x + \frac{\partial v}{\partial y} \Delta y \dots\dots\end{aligned}\quad (7)$$

where \tilde{x} and \tilde{y} are the positions of any points in deformed subsets. x and y are the positions of any points in undeformed subsets. u , $\frac{\partial u}{\partial x}$, $\frac{\partial u}{\partial y}$, v , $\frac{\partial v}{\partial x}$ and $\frac{\partial v}{\partial y}$ are displacements and displacement gradients at the center positions of subsets. The terms, $\Delta x = (x - x_p)$ and $\Delta y = (y - y_p)$, are the distances from subset centers to the points (x, y) .

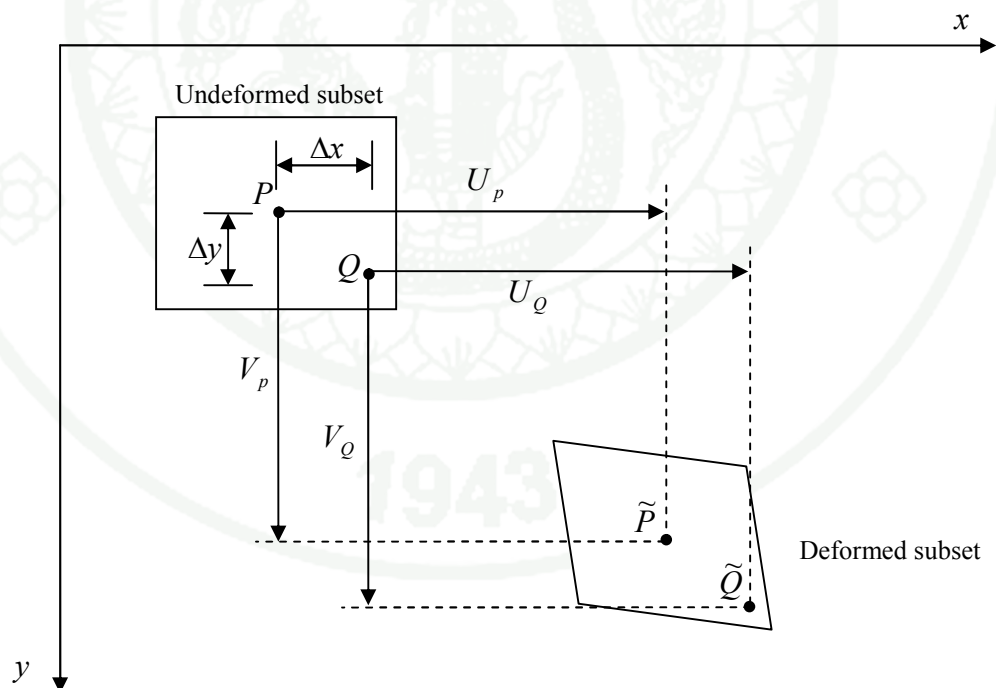


Figure 3 Mapping functions from undeformed and deformed subsets.

An image is a scalar function of the spatial coordinate that gives the gray values at each discrete point of coordinate (x, y) . The advection of the undeformed image $f(x, y)$ creates the deformed image $g(\tilde{x}, \tilde{y})$, such that

$$f(x, y) + b(x, y) = g(\tilde{x}, \tilde{y}) \quad (8)$$

where $b(x, y)$ is noise induced by image acquisition. Neglecting noise $b(x, y)$ can be made if noise's amplitude is low with respect to those of $f(x, y)$ and $g(\tilde{x}, \tilde{y})$. Equation (8) formulates a square of residual function:

$$R(x, y) = \sum_{S_p \in S} [f(x, y) - g(\tilde{x}, \tilde{y})]^2 \quad (9)$$

Let S represent all points in the subset, and let S_p represent any single point in the subset. Next, employing least square method compares the undeformed image and the deformed image. Then, eq. (9) can be rewritten as

$$\nabla R = \frac{\partial R}{\partial \mathbf{u}} = 0 \quad (10)$$

where vector \mathbf{u} is $\left[u, \frac{\partial u}{\partial x}, \frac{\partial u}{\partial y}, v, \frac{\partial v}{\partial x}, \frac{\partial v}{\partial y} \right]^T$ and ∇R is gradient of R . Equation (10) is

a system of nonlinear equation that can be solved by the Newton-Raphson method. The good initial guesses and iteration steps are required in the Newton-Raphson method. Therefore, eq. (10) solving by the Newton-Raphson method would be

$$\mathbf{u} = \mathbf{u}_0 - \{[\nabla \nabla R(\mathbf{u}_0)]^{-1} [\nabla R(\mathbf{u}_0)]\} \quad (11)$$

where the vector \mathbf{u}_0 is an initial guess of the solution and vector \mathbf{u} is the next iterative solution approximate solution of equation (10). $\nabla \nabla R(\mathbf{u}_0)$ is the second order

gradient of the square of residual function known as the Hessian matrix (Liu and Han, 2003). The convergence of this method faces with difficulty when the Hessian matrix is close to singular. While determinant of the Hessian matrix ($\nabla\nabla R$) is equal to zero, the Hessian matrix is not invertible.

In this study, the main purpose is to point out the importance of using sub-pixel algorithms for better accuracy than integer search methods. Both the simple search methods and N-R methods are written in MATLAB software. First, the accuracy of both methods is evaluated by using theoretical images of simple translation. Second, the measured displacements of cantilever beams are compared with elastic theory.

For translation simulation, creating synthetic images employs two following analytic functions (Bing et al., 2006):

$$\begin{aligned} f(x, y) &= \sum_{k=1}^s I_k^0 \exp \left[-\frac{(x-x_k)^2 + (y-y_k)^2}{R^2} \right] \\ g(\tilde{x}, \tilde{y}) &= \sum_{k=1}^s I_k^0 \exp \left[-\frac{[x-x_k-u_0-u_x x-u_y y]^2 + [y-y_k-v_0-v_x x-v_y y]^2}{R^2} \right] \end{aligned} \quad (12)$$

s is the total number of speckle granule, R is the size of the speckle granule and (x_k, y_k) are the central positions of each speckle granule with a random distribution, I_k^0 is the random peak intensity of each speckle granule. u_0 and v_0 are rigid body displacements in x and y directions. u_x and v_y are components of normal strains in x and y directions. u_y and v_x are components of shear strains in x and y directions. The theoretical images or synthetic images are useful because they have no needs for real experimental set-up. The virtual experimental set-up can be performed in computers which parameters such as speckle patterns, subset sizes, initial guesses and interpolation functions can be investigated before performing the actual experiments.

After investigating translation simulation by DIC, experiments of a cantilever beam are set-up to measure displacements in x and z directions as shown in figure 4. A digital camera (Olympus Camedia E-10) captures speckle images of undeformed and deformed cantilever beam. Systematic accuracy of DIC is evaluated by using analytical solutions derived from theory of elasticity.

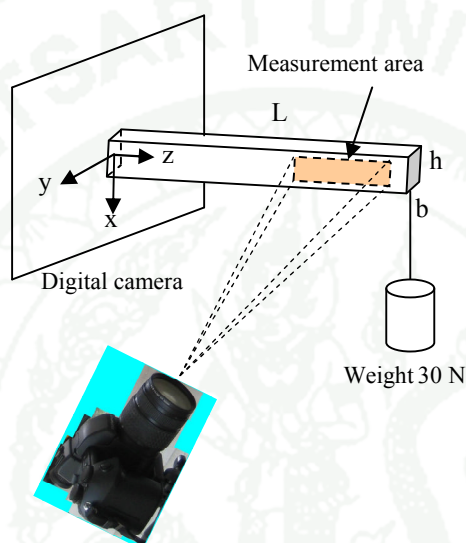


Figure 4 Experimental setup of the cantilever beam measured by DIC.

2. Identification of elastic material properties using MNET and DIC

The main goals of this study are to simulate all algorithms in figure 5 that apply for identifying material properties. In the previous works (Lecompte et. al., 2005, 2007), experiments of tensile tests on perforated specimens and biaxial tests on cruciform specimens have been performed very well but accuracy improvement is still required to investigate sources of errors in computer algorithms. Because those experiments are hardly performed to satisfy all conditions, analytical solutions are introduced to eliminate difficulty. In spite of experimental data, displacements from analytical data can also create speckle images in both undeformed stages and deformed stages.

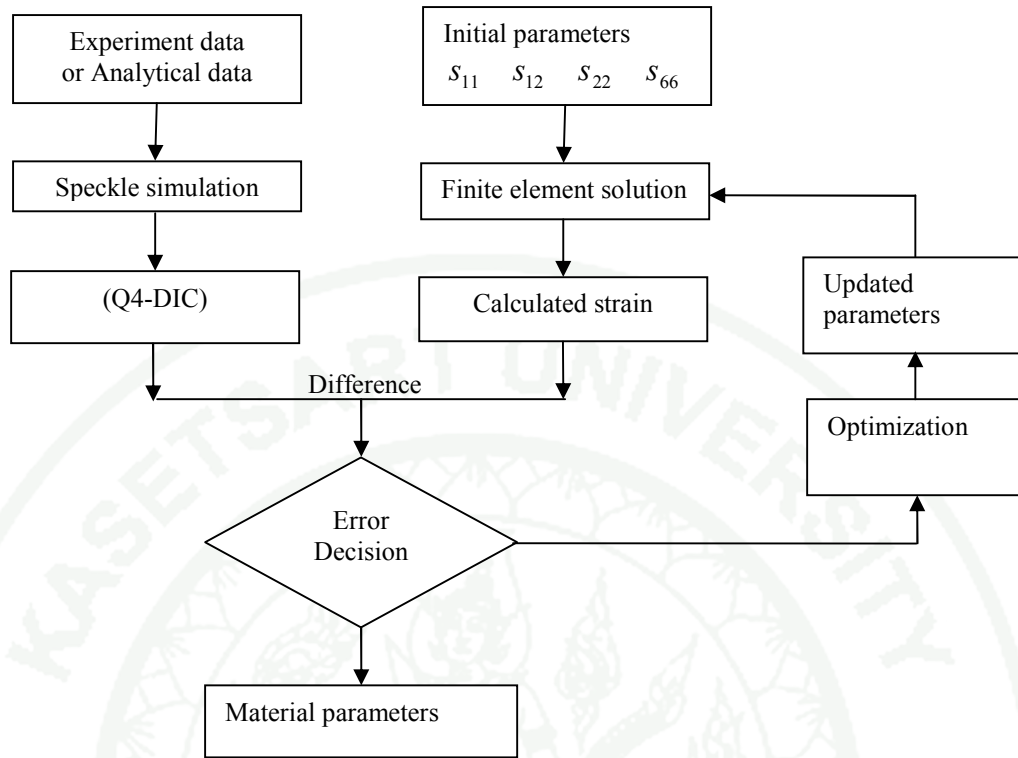


Figure 5 Flow-chart of MNET for identify material parameters.

2.1 Analytical solution of a plate with a circular hole

In figure 6, analytical solutions of an isotropic infinite plate with a circular hole subjected to uniaxial tensile loads are derived from Airy stress function (Barber, 2002; Sadd, 2009; Timoshenko and Goodier, 1969). Displacement fields in polar coordinates are given by

$$\begin{aligned}
 u_r &= \frac{Tr \cos 2\theta}{2E} \left[(1+\nu) + \frac{4a^2}{r^2} - (1+\nu) \frac{a^4}{r^4} \right] + \frac{Tr}{2E} \left[(1-\nu) + (1+\nu) \frac{a^2}{r^2} \right] \\
 u_\theta &= -\frac{Tr \sin 2\theta}{2E} \left[(1+\nu) + 2(1-\nu) \frac{a^2}{r^2} + (1+\nu) \frac{a^4}{r^4} \right]
 \end{aligned} \tag{13}$$

where T is stress or surface traction, E is Young's modulus and ν is Poisson's ratio. a is a radius of a central hole. The displacement transformation between polar coordinate and x-y coordinate can be written as

$$\begin{aligned} u(x, y) &= u_r \cos \theta - u_\theta \sin \theta \\ v(x, y) &= u_r \sin \theta + u_\theta \cos \theta \end{aligned} \quad (14)$$

where $u(x, y)$ is displacement in x-direction and $v(x, y)$ is displacement in y-direction. In this simulation, the displacements in eq. (14) are the baseline to calculate errors of MNET and DIC. A specimen in this simulation is a square rectangular plate 40×40 mm subjected to traction $T = 2$ MPa and it has a central hole radius of 2 mm. The thickness of the plate is 1 mm. The plate is made of polycarbonate with $E = 2.4$ GPa and $\nu = 0.45$.

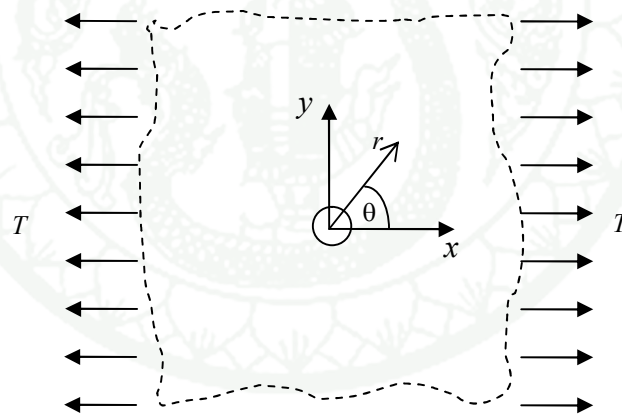


Figure 6 An infinite plate with a central hole.

2.2 Speckle simulation

Evaluating the DIC accuracy, computer-generated speckle images are more efficient methods to control speckle patterns. The quality of speckle sizes and distribution of speckle patterns are very crucial for DIC accuracy (Lecompte et. al., 2006). The displacements of analytical solutions in eq. (14) are used instead of finite

element simulation. Light intensity of each pixel in the image pairs of undeformed image $f(x,y)$ and deformed images $g(x',y')$ is generated by following analytic function (Bing et. al., 2006):

$$f(x,y) = \sum_{k=1}^s I_k^0 \exp\left[-\frac{(x-x_k)^2 + (y-y_k)^2}{R^2}\right]$$

$$g(x',y') = \sum_{k=1}^s I_k^0 \exp\left[-\frac{[x-x_k-u(x,y)]^2 + [y-y_k-v(x,y)]^2}{R^2}\right]$$
(15)

s is the total number of speckle granule, R is the size of the speckle granule and (x_k, y_k) are the central positions of each speckle granule with a random distribution, I_k^0 is the random peak intensity of each speckle granule from the normal distribution. The displacement functions, $u(x,y)$ and $v(x,y)$ in $g(x',y')$ are from analytical functions in eq.(14). Figure 7 (a) and (b) show example of the synthetic patterns for undeformed surfaces in ZOI and its histogram. The saturation problems of images can be checked by the histogram. The gray level of images is encoded on a 16-bit depth (0-65535 level) and the resolution of images is 0.04 mm per pixel.

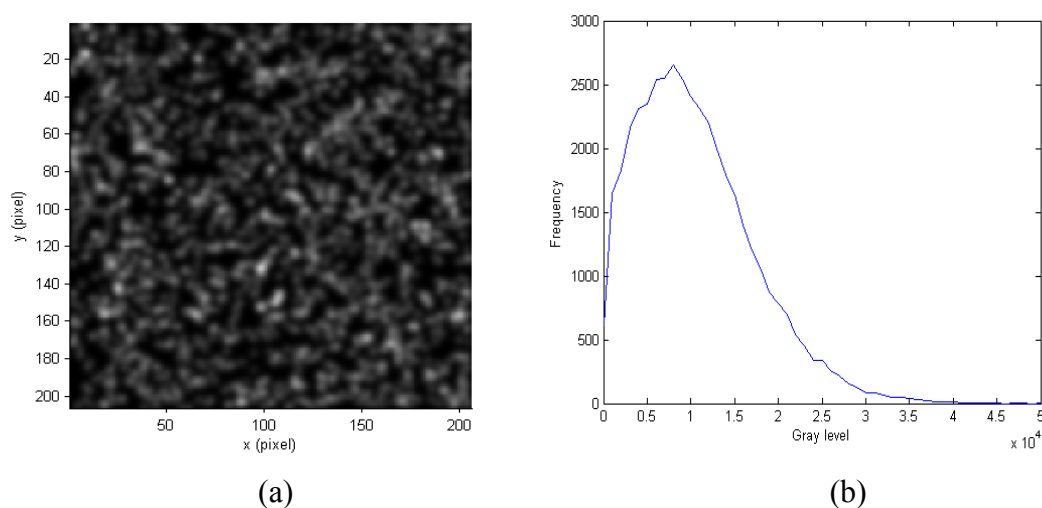


Figure 7 (a) Synthetic pattern of an undeformed image ($s=2000$, $R=3$, image size= 206×206 pixels,) (b) Histogram of gray levels on an undeformed image.

2.3 Q4-Digital image correlation (Q4-DIC)

The Q4-DIC technique (Besnard et al., 2006) is based on two images of specimen surfaces which are captured from digital cameras. The first image or reference image is in the undeformed stages. The second image or deform image is in the loading stages. Both images are scalar functions of spatial coordinates that represent the gray levels at each pixel. The reference images and deform images are called $f(\mathbf{x}')$ and $g(\mathbf{x})$. The conservation of optical flow (Horn and Schunck, 1981) can be expressed as

$$g(\mathbf{x}) = f[\mathbf{x} + \mathbf{u}(\mathbf{x})] \quad (16)$$

where $\mathbf{u}(\mathbf{x})$ is displacement of specimen surfaces. Let f and g be differentiable, and the displacement small enough, then Taylor expansion of f up to first order can be introduced to form residuals or errors as

$$R = g(\mathbf{x}) - f(\mathbf{x}) - \mathbf{u}(\mathbf{x}) \cdot \nabla f(\mathbf{x}) \quad (17)$$

In equation (17), bilinear quadrilaterals of finite element shape functions (Reddy, 2005) are introduced to approximate displacements:

$$\mathbf{u}(\mathbf{x}) = \Phi \mathbf{U} \quad (18)$$

where matrix Φ contains four element shape functions $(\phi_1, \phi_2, \phi_3, \phi_4)$ and matrix \mathbf{U} contains eight nodal displacements $(U_1, V_1, \dots, U_4, V_4)$. For local coordinate on a square $[0, 1]^2$, the four element shape functions are $(1-x)(1-y)$, $x(1-y)$, $y(1-x)$ and xy .

The zone of interest (ZOI) domain is defined as $\Omega \subset \mathfrak{R}^2$ that is divided into a small elemental domain Ω^e . Then, $\Omega^e \subset \Omega$ and least-square method requires the

integration of square residuals over Ω^e to be minimized with respect to unknown coefficients

$$\frac{\partial}{\partial \mathbf{U}} \int_{\Omega^e} R^2 d\Omega = 0. \quad (19)$$

Figure 8 (a) and (b) illustrates how to divide ZOI into elements and one element is divided into subsets Ω^s .

Minimizing eq.(19) in least square senses leads to systems of linear equation

$$\int_{\Omega^e} \mathbf{k}^T \mathbf{k} d\Omega \mathbf{U} = \int_{\Omega^e} \mathbf{k}^T (g - f) d\Omega. \quad (20)$$

where vector \mathbf{k} is $\left[\phi_1 \frac{\partial f}{\partial x}, \phi_1 \frac{\partial f}{\partial y}, \dots, \phi_4 \frac{\partial f}{\partial x}, \phi_4 \frac{\partial f}{\partial y} \right]_{1 \times 8}$. The reference image gradients in x and y direction are $\frac{\partial f}{\partial x}$ and $\frac{\partial f}{\partial y}$ respectively, that determine from grayscale interpolation of each pixel.

Equation (20) may be written in a compact form as

$$\mathbf{K}^e \mathbf{U}^e = \mathbf{F}^e \quad (21)$$

The element matrices \mathbf{K}^e and \mathbf{F}^e that can be assembled to form a global stiffness matrix \mathbf{K} and force vector \mathbf{F} as in finite element problems. The global stiffness matrix \mathbf{K} is symmetric, square and sparse. Ill condition can be occurred if reference image gradients are small.

Both fast fourier transform (FFT) and bi-cubic spline have been studied to reconstruct images for sub-pixel interpolation. The advantages of FFT are rapid

computation and providing smooth C_∞ for interpolated functions. On the other hand, fourier transform can creates undesired oscillation for image edges and sharp differences of image gradients. The computation of bicubic spline is rather time-consuming but high accuracy can be obtained from this interpolation. In this work, bicubic splines are provided sub-pixel accuracy for DIC algorithm.

To construct bi-cubic spline in undeformed images and deform images, interpolation functions are used in an element. The bicubic spline functions on a square local coordinate $[-1/2, 1/2]^2$ can be written in polynomial forms (Lancaster and SAlkauskas, 1986):

$$\begin{aligned} f(\tilde{x}, \tilde{y}) &= \sum_{i=0}^3 \sum_{j=0}^3 a_{ij} \tilde{x}^i \tilde{y}^j \\ g(\tilde{x}, \tilde{y}) &= \sum_{i=0}^3 \sum_{j=0}^3 b_{ij} \tilde{x}^i \tilde{y}^j \end{aligned} \quad (22)$$

where a_{ij} and $b_{i,j}$ are spline coefficients that need to determine. For example, a_{ij} of $f_1(\tilde{x}, \tilde{y})$ can be computed by solving linear system equation:

$$\mathbf{A} \cdot \mathbf{b} = \mathbf{C} \quad (23)$$

where vector \mathbf{b} size 16×1 contains spline coefficients $[a_{00}, a_{10}, a_{20}, \dots, a_{33}]^T$ and vector \mathbf{C} size 16×1 contains gray values and its gradients $(f, \frac{\partial f}{\partial \tilde{x}}, \frac{\partial f}{\partial \tilde{y}}, \frac{\partial^2 f}{\partial \tilde{x} \partial \tilde{y}})$ in four node positions $(-1/2, -1/2)$, $(1/2, -1/2)$, $(-1/2, 1/2)$ and $(1/2, 1/2)$. Finite Differences is helpful to calculate gradients $(\frac{\partial f}{\partial \tilde{x}}, \frac{\partial f}{\partial \tilde{y}}, \frac{\partial^2 f}{\partial \tilde{x} \partial \tilde{y}})$ for each pixel. The matrix \mathbf{A} size 16×16 contains coefficients by substituting node positions into \tilde{x} and \tilde{y} of eq.(2.10).

Performing integration of eq.(20) cannot be evaluated directly because one element consists of many subsets Ω^s of spline functions. The local coordinates of elements are substituted by local coordinates of spline functions that have the centers at spline squares. Therefore, area integrals of an element in right hand and left hand of eq.(20) can be written with the change of variables (Zill and Wright, 2011) to reduce integration terms as follows:

$$\int_{\Omega^e} \mathbf{k}^T \mathbf{k} d\Omega = \sum_{i=1}^n \int_{\Omega_i^s} \mathbf{k}^T \mathbf{k} \det \mathbf{J} d\Omega \quad (24)$$

$$\int_{\Omega^e} \mathbf{k}^T (g - f) d\Omega = \sum_{i=1}^n \int_{\Omega_i^s} \mathbf{k}^T (g - f) \det \mathbf{J} d\Omega$$

where i is numbers of spline functions from 1 to n in an element and \mathbf{J} is 2×2 Jacobian matrix.

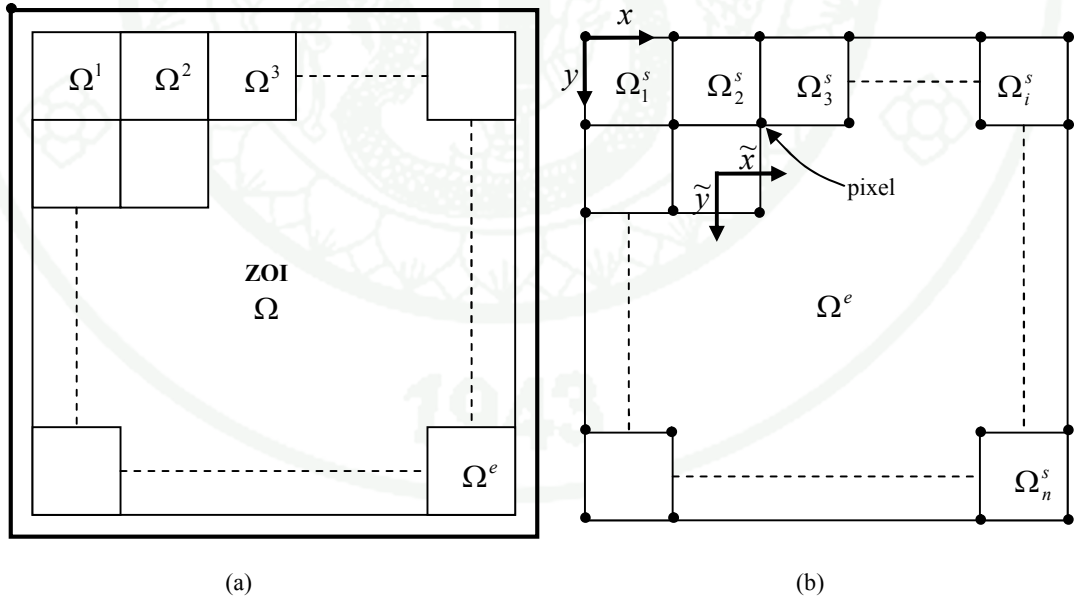


Figure 8 (a) ZOI domain Ω consisting of many element domains, (b) one elemental domain Ω^e consisting of many subsets Ω^s of spline functions.

2.4 Finite element methods

The governing equation and boundary condition for orthotropic plane linear elasticity problems (Burnett, 1987; Reddy, 2005) are summarized below.

$$-\nabla \cdot \boldsymbol{\sigma} = \mathbf{f} \quad \text{in} \quad \Omega \quad (25)$$

$$\mathbf{u} = \mathbf{u}_D \quad \text{on} \quad \partial\Omega_D \quad (26)$$

$$\boldsymbol{\sigma} \cdot \mathbf{n} = \mathbf{t}_N \quad \text{on} \quad \partial\Omega_N \quad (27)$$

Assume that $\Omega \subset \mathbf{R}^d$ ($d = 2$) is a bounded polygon. $\boldsymbol{\sigma}$ and \mathbf{f} denote the symmetric Cauchy stress tensor and the body force. $\nabla \cdot$ is a divergence operator. \mathbf{u}_D is the prescribed displacement on Dirichlet boundary, $\partial\Omega_D$ and \mathbf{t}_N is the prescribed traction vector on Neumann boundary, $\partial\Omega_N$. The constitutive equations ($\boldsymbol{\sigma} = \mathbf{c} : \boldsymbol{\varepsilon}$) for finite element models uses orthotropic stiffness elastic materials. Formulation plane elastic problem using eq. (25), (26) and (27) with constitutive equation obtains stiffness matrix, force matrix and displacement matrix. The picture in figure 9 (a) is 2127 triangular elements of finite element mesh with 1116 nodes and figure 9 (b) is boundary condition for finite element models. Finite element strains from ZOI use for optimization with DIC strains in the next section. The ZOI are studied for the errors and convergences of the current set-up of DIC and MNET.

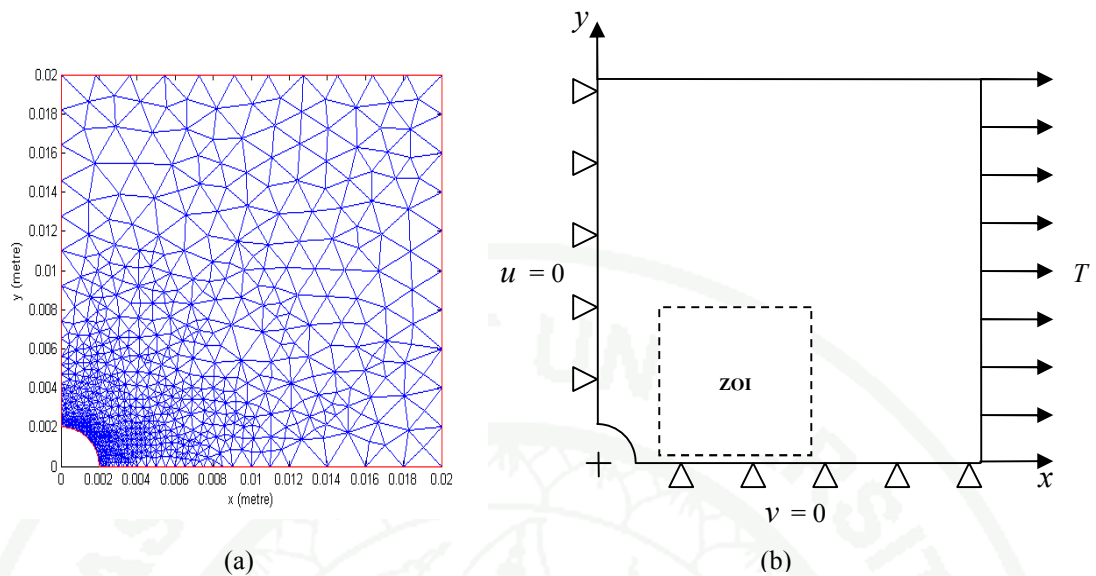


Figure 9 (a) FEM mesh (b) FEM boundary condition and ZOI (size = 0.00825 m²).

The analytical solution in eq.(14) is based on an infinite plate while the FEM solution is based on finite plate. Before doing further analysis, the discrepancy between the analytical model and the FEM model must be verified by using relative errors in L₂-norm of displacements to ensure minimum bias (Akin, 2005). The relative errors in L₂-norm can be defined as

$$\frac{\|U^{exact} - U^{FEM}\|_0}{\|U^{FEM}\|_0} = \frac{\sqrt{\sum_i (U_i^{exact} - U_i^{FEM})^2}}{\sqrt{\sum_i (U_i^{exact})^2}} \quad (28)$$

where i is number of FEM nodes. U_i^{exact} and U_i^{FEM} are the analytical displacements and FEM displacements. The various FEM models that have different mesh configuration and mesh sizes are compared to the analytical model for resemblance. Finally, the FEM mesh configuration in fig. 9(a) is selected with minimum bias and the relative errors in L₂-norm for this mesh configuration is equal to 0.0049 (or 0.49%) for displacements in x-direction and 0.0146 (or 1.46%) for displacements in y-direction.

2.5 Optimization in inverse methods

The identification of material parameters is based on a Gauss-Newton optimization method (Björck, 1996). When least square method is formed a residual function (R) in eq.(29), it measures the differences of DIC strain and FEM strain. In the residual function, the different strains of n triangular elements of FEM are added together and they are linearised by Taylor expansion around four unknown parameters (s_{11}, s_{12}, s_{22} and s_{66}). Finally, residual function is subsequently minimized with respect to four unknowns. The least square residual function can be expressed as

$$R(\underline{s}) = \sum_{i=1}^n \left[(\varepsilon_x^{FEM}(\underline{s}) - \varepsilon_x^{DIC})^2 + (\varepsilon_y^{FEM}(\underline{s}) - \varepsilon_y^{DIC})^2 + (\gamma_{xy}^{FEM}(\underline{s}) - \gamma_{xy}^{DIC})^2 \right] \quad (29)$$

where finite element strains are ε_x^{FEM} , ε_y^{FEM} and γ_{xy}^{FEM} and DIC strains are ε_x^{DIC} , ε_y^{DIC} and γ_{xy}^{DIC} . The unknown vector ($\underline{s} = [s_{11}, s_{12}, s_{22}, s_{66}]$) is to be identified by minimizing residual function,

$$\frac{\partial R(\underline{s})}{\partial s_j} = 0 \quad (30)$$

where j is 11, 12, 22 and 66. Then, there are four equations to be solved.

The Taylor expansion is

$$\varepsilon_x^{FEM}(\underline{s}) \cong \varepsilon_x^{FEM}(\underline{s}^k) + \sum_{j=11,12,22,66} \frac{\partial \varepsilon_x^{FEM}(\underline{s})}{\partial s_j} (s_j - s_j^k) \quad (31)$$

which ε_y^{FEM} and γ_{xy}^{FEM} can be formulated as same as ε_x^{FEM} . The term $(s_j - s_j^k)$ is the difference between the initial value s_j^k at point k and its new estimate s_j . Finally, updated parameters can be obtained by solving

$$\underline{\Delta s} = (\mathbf{A}^t \mathbf{A})^{-1} \mathbf{A}^t \left(\underline{\varepsilon}^{DIC} - \underline{\varepsilon}^{FEM} (\underline{s}^k) \right) \quad (32)$$

where $\underline{\Delta s}$ is a column vector of the updated parameter ($\Delta s_{11}, \Delta s_{12}, \Delta s_{22}$ and Δs_{66}),

\mathbf{A} is sensitivity matrix containing strain gradients,

$\underline{\varepsilon}^{DIC}$ is a column vector of DIC strains ($\varepsilon_x^{DIC}, \varepsilon_y^{DIC}$ and γ_{xy}^{DIC}),

$\underline{\varepsilon}^{FEM}$ is a column vector of FEM strains ($\varepsilon_x^{FEM}, \varepsilon_y^{FEM}$ and γ_{xy}^{FEM}) at iteration k,

\underline{s}^k is the four compliance coefficients.

The sensitivity matrix \mathbf{A} can be derived from the constitutive equation for orthotropic plane stress:

$$\begin{Bmatrix} \varepsilon_x^{FEM} \\ \varepsilon_y^{FEM} \\ \gamma_{xy}^{FEM} \end{Bmatrix} = \begin{bmatrix} s_{11} & s_{12} & 0 \\ s_{12} & s_{22} & 0 \\ 0 & 0 & s_{66} \end{bmatrix} \begin{Bmatrix} \sigma_x \\ \sigma_y \\ \tau_{xy} \end{Bmatrix} \quad (33)$$

For isotropic plane stress, $s_{11} = s_{22}$. In this work, both isotropic constitutive equations and orthotropic constitutive equations are studied to identify isotropic material properties that are generated from analytical solution.

The DIC Strains ($\varepsilon_x^{DIC}, \varepsilon_y^{DIC}$ and γ_{xy}^{DIC}) are computed from quadrilateral interpolation generating displacements at triangular nodes of FEM as figure 10. Next, strains can be calculated by differentiating displacement triangular shape functions.

$$\varepsilon_x^{DIC} = \frac{\partial \phi_1}{\partial x} u_1 + \frac{\partial \phi_2}{\partial x} u_2 + \frac{\partial \phi_3}{\partial x} u_3 \quad (34)$$

The displacements (u_1, u_2 and u_3) in eq.(34) are computed from Q4 elements:

$$u_1 = u^{DIC}(x_1, y_1) = \phi_i(x_1, y_1)u_i + \phi_j(x_1, y_1)u_j + \phi_m(x_1, y_1)u_m + \phi_n(x_1, y_1)u_n \quad (35)$$

The values of ε_y^{DIC} and γ_{xy}^{DIC} also are calculated the same procedures as ε_x^{DIC} .

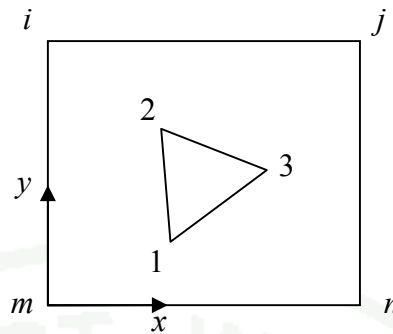


Figure 10 Computing DIC strains from Q4 elements and triangular elements.

The decision to stop iterations uses percent relative errors defined as

$$e_j = \left| \frac{s_j^k - s_j}{s_j^k} \right| \times 100 \quad j = 11, 12, 22, 66 \quad (36)$$

where s_j^k is the compliance coefficient for the present iteration and s_j is the compliance coefficient for the previous iteration. When all relative errors (e_j) are less than 0.01 %, the iterations will be terminated.

3. Optical flow and discontinuous finite element formulation

Where the problems with discontinuous displacements are involved such material cracks and sliding interfaces, the continuous bases of optical flow face with difficulty to detect discontinuous displacements. For recent advances in computational mechanics, an extended digital image correlation (X-DIC) is introduced using partition of unity method to solve the discontinuous problems. For X-DIC, the study domain Ω is separated by the support of the discontinuity Γ into two parts Ω^- and Ω^+ . In this section, an alternative approach based on optical flows and discontinuous finite element methods is introduced to solve discontinuity problems.

3.1 1-D of continuous finite element methods for optical flows

The conservation of optical flow in 2-D presented by eq.(16) can be reduced to one dimension as

$$g(x) = f(x + u(x)) \quad (37)$$

where the function $f(x)$ represents grey values in the reference image and the function $g(x)$ represents grey values in the deform image. The function $u(x)$ is a displacement function. Next, the Taylor expansion of $f(x + u(x))$ can be introduced into eq.(37) and the residual function can be formed as

$$R = f(x) + u(x) \frac{\partial f(x)}{\partial x} - g(x) \quad (38)$$

In equation (38), one-dimensional linear shape functions (Reddy, 2005) are introduced to approximate displacements

$$u(x) = \phi_i U_i + \phi_j U_j \quad (39)$$

where element shape functions are $\phi_i = (1 - x)$ and $\phi_j = x$. The nodal displacements are U_i and U_j . In least square method, seeking minimum square residuals requires

$$\frac{\partial}{\partial \mathbf{U}} \left(\int_{x_i}^{x_j} R^2 dx \right) = 0 \quad (40)$$

where vector \mathbf{U} is $[U_i, U_j]$. Minimizing eq.(39) in least square senses leads to systems of linear equation

$$\int_{x_i}^{x_j} \mathbf{k}^T \mathbf{k} dx \mathbf{U} = \int_{x_i}^{x_j} \mathbf{k}^T (g - f) dx . \quad (41)$$

where vector \mathbf{k} is $\left[\phi_i \frac{\partial f}{\partial x}, \phi_j \frac{\partial f}{\partial x} \right]$. The reference image gradient is $\frac{\partial f}{\partial x}$ that determine from grayscale interpolation of each pixel.

Equation (20) may be written in a compact form as

$$\mathbf{K}^e \mathbf{U}^e = \mathbf{F}^e \quad (42)$$

The element matrices \mathbf{K}^e and \mathbf{F}^e that can be assembled to form a global stiffness matrix \mathbf{K} and force vector \mathbf{F} as in finite element problems. The global stiffness matrix \mathbf{K} is symmetric, square and sparse. Ill condition can be occurred if reference image gradients are small.

To construct hermite spline in undeformed images and deform images, interpolation functions are used in an element. The hermite spline functions on local coordinate can be written in polynomial forms (Lancaster and SAlkauskas, 1986):

$$\begin{aligned} f(\tilde{x}) &= \sum_{i=0}^3 a_i \tilde{x}^i \\ g(\tilde{x}) &= \sum_{i=0}^3 b_i \tilde{x}^i \end{aligned} \quad (43)$$

where a_i and b_i are spline coefficients that need to determine. For example, a_i of $f_1(\tilde{x})$ can be computed by solving linear system equation:

$$\mathbf{A} \cdot \mathbf{b} = \mathbf{C} \quad (44)$$

where vector \mathbf{b} size 4×1 contains spline coefficients $[a_0, a_1, a_2, a_3]^T$ and vector \mathbf{C} size 4×1 contains gray values and its gradients $(f, \frac{\partial f}{\partial \tilde{x}})$ in two node positions $\tilde{x} = -1/2$ and $\tilde{x} = 1/2$. Finite Differences is helpful to calculate gradients $(\frac{\partial f}{\partial \tilde{x}})$ for each pixel. The matrix \mathbf{A} size 4×4 contains coefficients by substituting node positions into \tilde{x} and \tilde{y} of eq.(42).

Performing integration of eq.(40) cannot be evaluated directly because one element consists of many subsets Ω^s of spline functions. The local coordinates of elements are substituted by local coordinates of spline functions that have the centers at spline squares. Therefore, area integrals of an element in right hand and left hand of eq.(40) can be written with the change of variables (Zill and Wright, 2011) to reduce integration terms as follows:

$$\begin{aligned} \int_{x_i}^{x_j} \mathbf{k}^T \mathbf{k} dx &= \sum_{i=1}^n \int_{\tilde{x}_i}^{\tilde{x}_j} \mathbf{k}^T \mathbf{k} \frac{dx(\tilde{x})}{d\tilde{x}} d\tilde{x} \\ \int_{x_i}^{x_j} \mathbf{k}^T (g - f) dx &= \sum_{i=1}^n \int_{\tilde{x}_i}^{\tilde{x}_j} \mathbf{k}^T (g - f) \frac{dx(\tilde{x})}{d\tilde{x}} d\tilde{x} \end{aligned} \quad (45)$$

where i is numbers of spline functions from 1 to n in an element.

3.2 1-D of discontinuous finite element methods for optical flows

To illustration the basic ideas of the discontinuous least square finite element method, the derivation follows in the book (Li, 2010). Least square methods from eq.(39) can be expressed as

$$\int \left(\frac{\partial R}{\partial \mathbf{U}} \right) R dx = 0 \quad (46)$$

Let $\mathbf{W} = \frac{\partial R}{\partial \mathbf{U}}$, then eq.(39) can be rewritten as

$$\int \mathbf{W} \left(\mathbf{U} \frac{\partial f}{\partial x} + f - g \right) dx = 0 \quad . \quad (47)$$

Performing integration by parts two times of eq.(46), a discontinuous element formulation can be constructed by weakly imposed boundary conditions across element boundary. Then, eq.(46) is written with terms of a jump across the element boundary,

$$\int_{x_i}^{x_j} \mathbf{W} \mathbf{U} \frac{\partial f}{\partial x} dx + \mathbf{W}(x_i^+) \mathbf{U}(x_i^+) f(x_i^+) - \mathbf{W}(x_i^-) \mathbf{U}(x_i^-) f(x_i^-) = \int_{x_i}^{x_j} \mathbf{W}(g - f) dx \quad (48)$$

The integration terms in eq.(48) requires change of variable and summation of spline function as in eq.(45). The numerical simulation based on the separation movement of two objects is illustrated in figure 11.

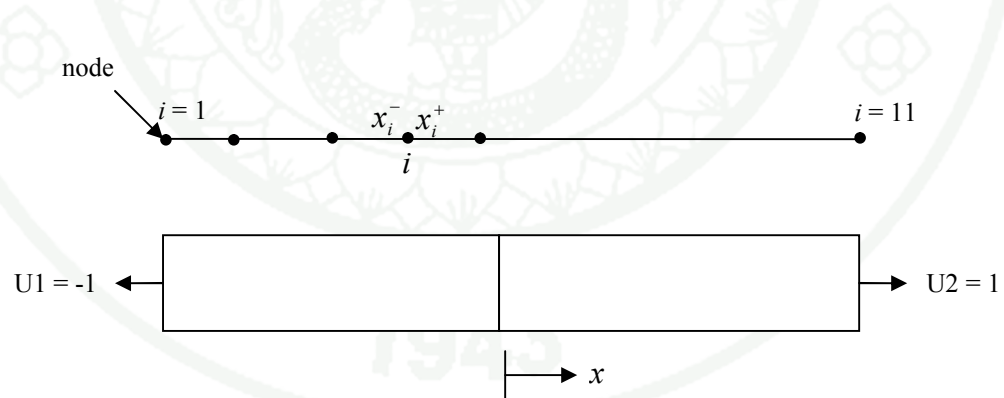


Figure 11 Separation movement of two objects and their displacements.

RESULTS AND DISCUSSIONS

1. Study DIC algorithm

The synthetic images of speckle patterns are created from equation (12). The number of speckle granules $s = 500$ and the sizes of speckle granule $R = 4$ are applied to equation (12). The random peak intensity of each speckle granule (I_k^0) that has a range between 0 and 255. For rigid body translation, there is no strain so that all strain values (u_x , u_y , v_x and v_y) should be zero. A series of synthetic speckle images shown as figure 12 is generated by the computer program with the displacements (u_0 and v_0) ranging from 0 to 2 pixel, corresponding to a shift of 0.1 pixels between two consecutive images. Figure 12 (a) and (b) are undeformed and deformed synthetic images that have the image sizes of 250×250 pixels. The displacements are calculated at the center subsets that have the sizes 41×41 pixels.

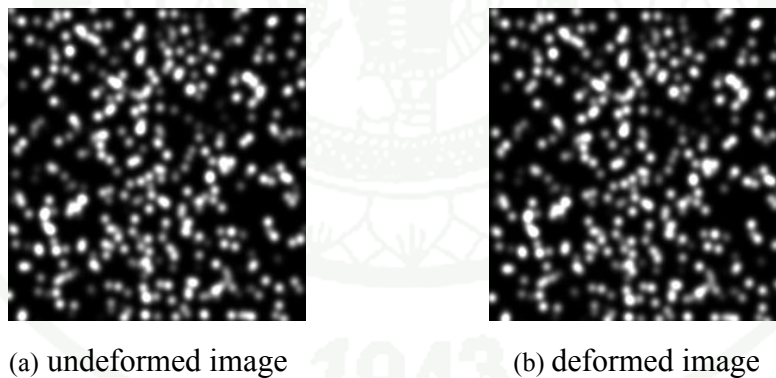


Figure 12 Synthetic speckle patterns of (a) undeformed image (b) deformed image with $u_0 = 2, v_0 = 2, u_x = v_y = v_x = u_y = 0$.

The accuracy of DIC may be evaluated by comparing the resultant vectors of pre-imposed displacements (d_{sim}) and the resultant vectors of measured displacements (d_{DIC}). The percentage displacement errors can be defined as

$$\% \text{ error} = \frac{|d_{sim} - d_{DIC}|}{d_{sim}} \times 100 \quad (49)$$

where $d_{sim} = \sqrt{u_0^2 + v_0^2}$ and $d_{DIC} = \sqrt{u^2 + v^2}$. The displacements u_0 and v_0 are the component vectors in x and y directions of the pre-imposed displacement vectors (d_{sim}). The displacements u and v are the component vectors in x and y directions of the measured displacement vectors (d_{DIC}). In figure 13, 21 points of percentage displacement errors are plotted against the pre-imposed displacements (d_{sim}). In this study, the sub-pixel algorithm is N-R algorithm. The percentage errors of DIC using sub-pixel algorithm (%error1) is less than errors of simple search algorithms (%error2).

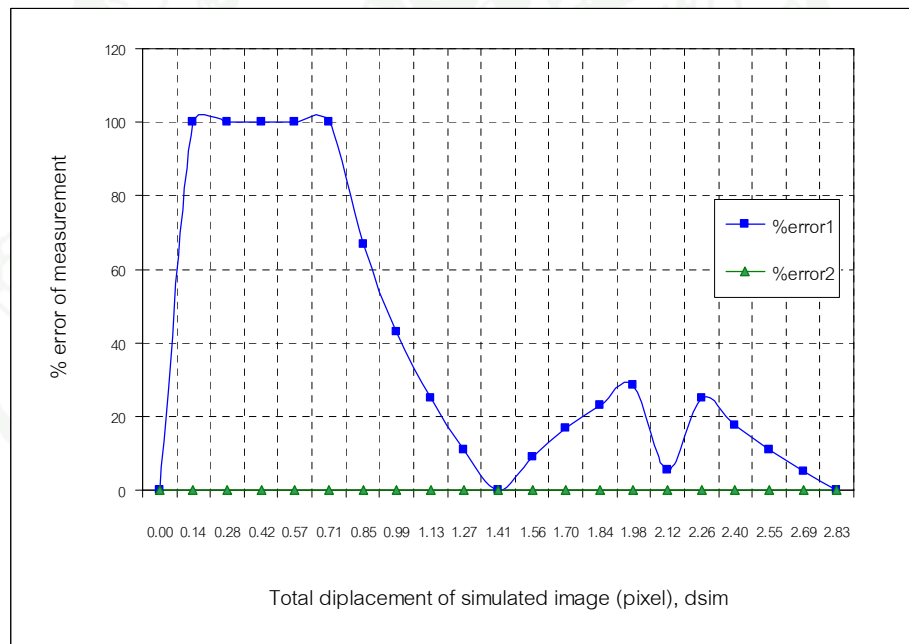


Figure 13 Percentage errors of DIC measurements, %error1 (no sub-pixel), %error2 (with sub-pixel).

Next, a simple search algorithm of DIC is applied to measure deflection of an experiment of cantilever beam. The elastic theory of cantilever beam is utilized to evaluate accuracy of the algorithm (Timoshenko and Goodier, 1969). In figure 14, a steel cantilever beam that is subjected to a force 30 N caused bending moment at the beam tip. The beam has dimension $160 \times 12 \times 4$ mm ($L \times b \times h$). u and w displacements in x and z directions can be obtained from analytical equations:

$$u = \frac{M}{2EI_y} [z^2 + \nu(x^2 - y^2)]$$

$$w = \frac{M}{EI_y} xz$$
(50)

where the modulus of elasticity (E) and Poisson's ratio (ν) are 200 GPa and 0.3, respectively. I_y is moment of inertia that is 6.4×10^{-11} m⁴. x , y and z are the positions on the cantilever beam. In this experiment, displacements are measured in the middle of the beam height ($x = 0$), the middle of the beam width ($y = b/2$) and six positions on the beam length ($z = 10, 11, 12, 13, 14$ and 15 cm). The image resolution that is calculated from camera resolution and object length is 26.3 pixel / m.

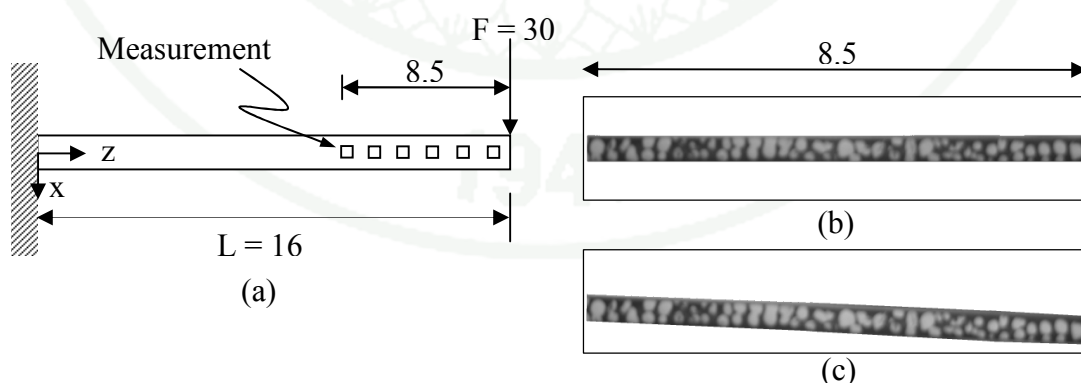


Figure 14 Deformation of cantilever beam (a) measurement positions (b) image of undeformed beam (c) image of deformed beam.

The analytical displacements from equation (49) are compared with simple search methods of DIC. Figure 14(a) displays the measurement position on the cantilever beam. Figure 14(b) and figure 14(c) display the undeformed image and the deformed image that captured by a digital camera. The undeformed images or template images corresponding to measurement positions have the image sizes 141×91 pixels. The cross-correlation coefficients are computed to find the best matching of template images and undeformed image. The ZOI sizes for searching are 151×331 pixels. Table 1 is the displacement results of DIC measurements compared with displacement values from elastic theory. For this setup, the difference between DIC measurements and elastic theory of beam bending is in the ranges of 0.08-0.2 mm.

Table 1 Comparison of theory displacements and measured displacements.

Distance on z-axis , (cm)	Displacement u , (mm)			Displacement w , (mm)		
	Theory	DIC	Difference	Theory	DIC	Difference
15	4.0165	4.1777	-0.1612	0	0.1140	-0.1140
14	3.6729	3.7333	-0.0604	0	0.1520	-0.1520
13	3.1667	3.3777	-0.2110	0	0.1520	-0.1520
12	2.6979	2.9333	-0.2354	0	0.1520	-0.1520
11	2.2667	2.4444	-0.1777	0	0.1520	-0.1520
10	1.8729	1.9555	-0.0826	0	0.1520	-0.1520

2. Identification of elastic material properties using MNET and DIC

The analytical solutions in eq.(14) generate displacements, $u(x, y)$ and $v(x, y)$, to create speckle images using eq. (15). The pairs of artificial images, undeformed images and deformed images, are measured for displacements by Q4-DIC. The sizes of ZOI are 206×206 pixels that are divided into 29 elements and 900 nodes with subset 8×8 pixels per element. The selections of ZOI sizes and number of elements depend on a trade-off between CPU time and measurement resolution. The DIC displacements from ZOI in figure 9(b) are examined for errors. For

displacements in x-direction, the error criterion of each ZOI are relative errors in the L_2 -norm defined as

$$\frac{\|U^{exact} - U^{DIC}\|_0}{\|U^{exact}\|_0} = \frac{\sqrt{\sum_{n=1}^{900} (U_n^{exact} - U_n^{DIC})^2}}{\sqrt{\sum_{n=1}^{900} (U_n^{exact})^2}} \quad (51)$$

where n is number of DIC nodes on ZOI. U_n^{exact} and U_n^{DIC} are the analytical displacements and DIC displacements in x-axis of each node. The relative errors in the L_2 -norm for displacements in y-direction, $\frac{\|V^{exact} - V^{DIC}\|_0}{\|V^{exact}\|_0}$, can be calculated the

same procedures as the relative errors in the L_2 -norm for displacements in x-direction. The relative errors and the percent relative errors in L_2 -norm are summarized in table 2.

Figure 15 (a) and (b) are u and v displacements from analytical solutions on ZOI. The results of DIC measurements are figure 15 (c) and (d) that show a good agreement with analytical displacements. However, there are some high errors of u and v displacements that are close to x and y axis. One cause of errors is from nonlinear displacements that are hardly measured by DIC. The DIC displacements contain some numerical noises that affect DIC strain calculation. In this work, noisy strains are applied directly to identify elastic constants.

Table 2 Relative errors in L_2 -norm of U and V displacements on ZOI.

	$\frac{\ U^{exact} - U^{DIC}\ _0}{\ U^{exact}\ _0}$	$\frac{\ V^{exact} - V^{DIC}\ _0}{\ V^{exact}\ _0}$
Relative errors in L_2 -norm	0.0258 (2.58%)	0.0594 (5.94%)

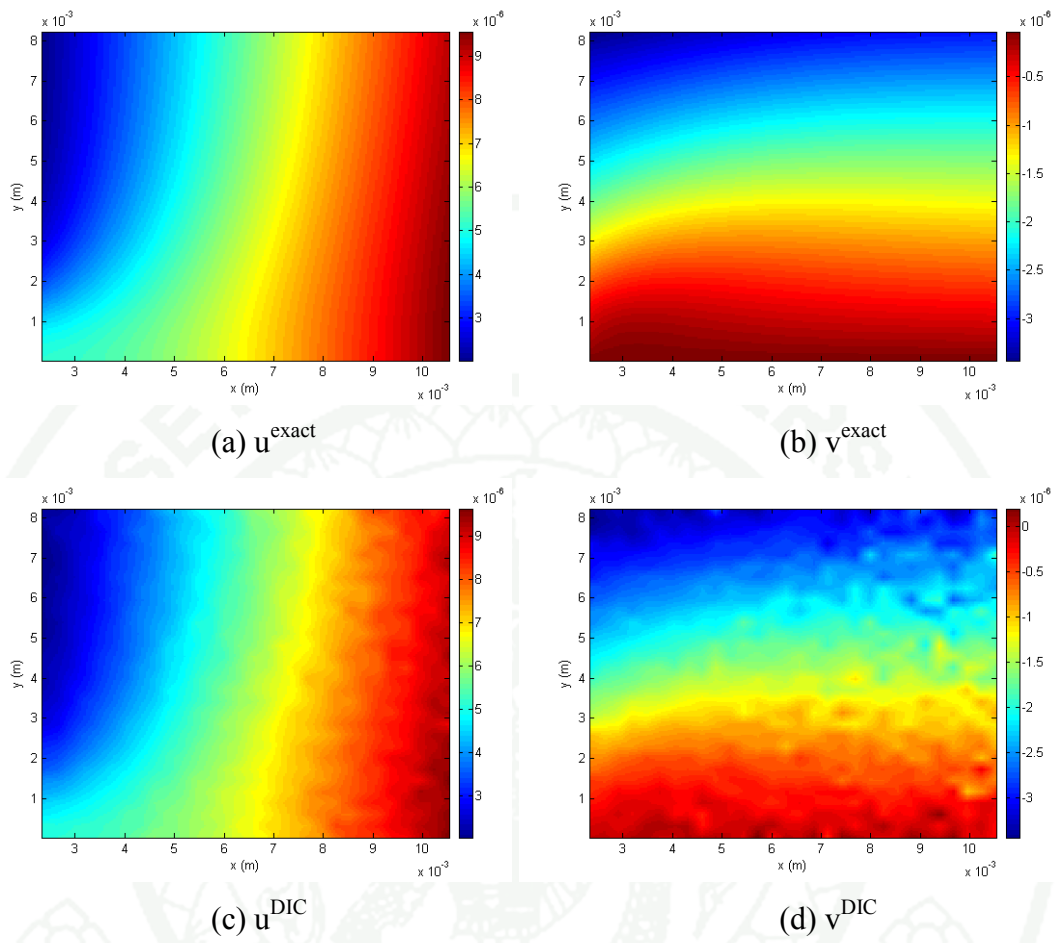


Figure 15 DIC x-y analytical displacement (a), (b) and x-y DIC displacement (c), (d) on ZOI.

1943

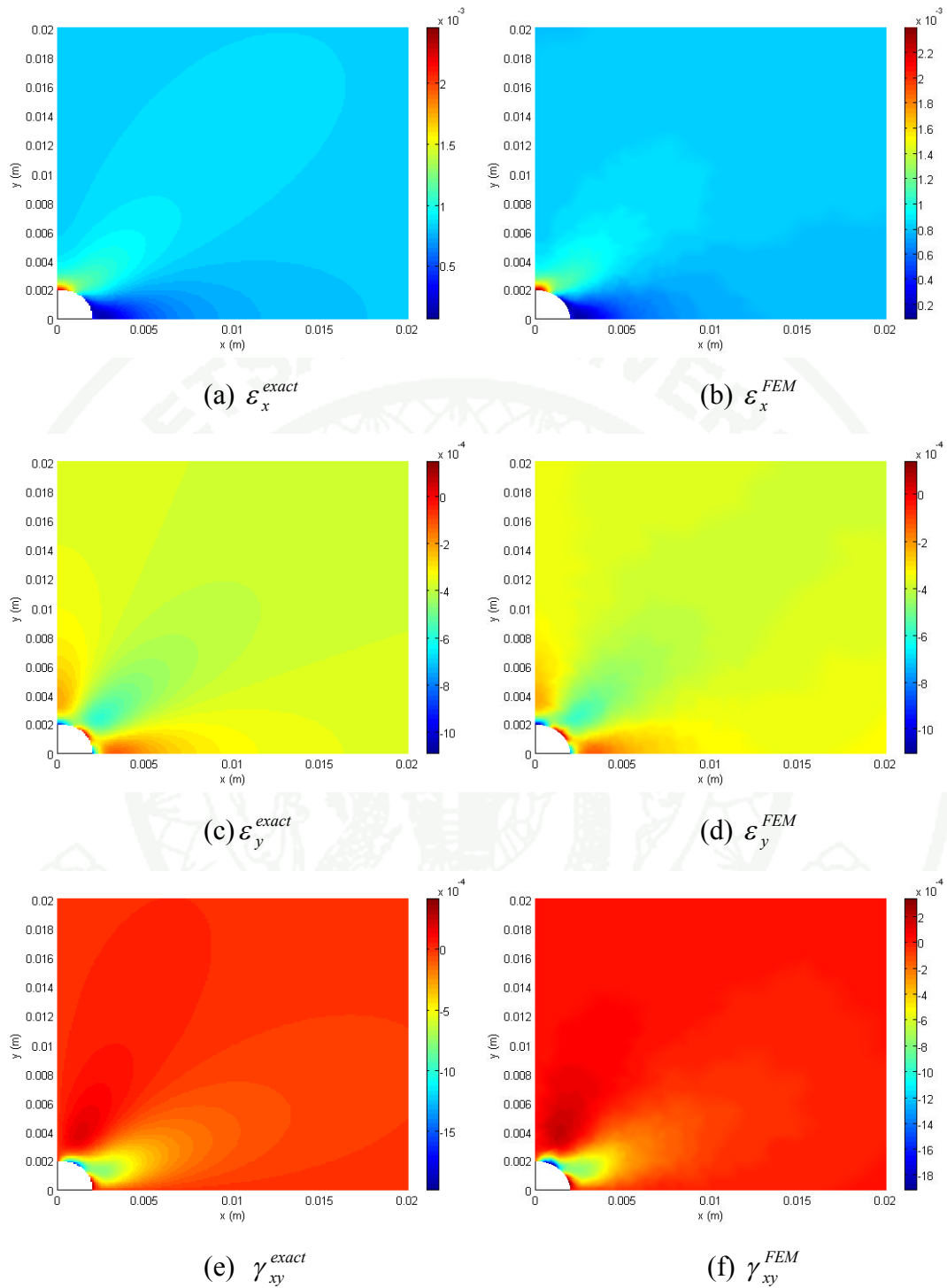


Figure 16 Analytical strains (a), (c), (e) and FEM strains (b), (d), (f)

In optimization routine, the DIC strains and FEM strains are compared iteratively by using least square methods to find the best matches of four compliance coefficients. Ten pairs of artificial images, undeformed images and deformed images, are measured for displacements by Q4-DIC. The convergences of updated compliance coefficients are achieved about 5th iteration for isotropic models and 9th for orthotropic models. The corrupted noisy strains from DIC strains are reconstructed by FEM for the whole specimens in figure 16 (b, d and f). The relative errors between analytical strains in figure 16 (a, c and e) and finite element strains in figure 16 (b, d and f) can be observed for model validation purposes.

Two material models that are isotropic models and orthotropic models are studied for identification accuracy of elastic coefficients. The imposed coefficients of polycarbonate materials from analytical solution act as a baseline to quantify errors of these identification procedures. For isotropic parameters in table 3, Young's modulus (E), Poisson ratio (ν) and shear modulus (G) from virtual experiments are compared with imposed values. For orthotropic parameters in table 4, there are also some unbalance values of E_x and E_y .

Table 3 Elastic coefficients using isotropic model.

	E (GPa)	ν	G (GPa)
Initial guess	1.00	0.5000	-
Exact value	2.40	0.4500	0.82759
Average	2.46	0.4651	0.83899
Standard deviation	0.0135	0.0037	0.00246
Percentage error (%)	3.25	2.38	1.35

Table 4 Elastic coefficients using orthotropic model.

	E_x (GPa)	E_y (GPa)	ν_{xy}	G_{xy} (GPa)
Initial guess	1.00	1.00	0.5000	1.00000
Exact value	2.40	2.40	0.4500	0.82759
Average	2.46	2.19	0.4594	0.82758
Standard deviation	0.0129	0.1597	0.0073	0.01646
Percentage error (%)	2.46	8.83	2.08	0.00036

2.1 Discussion

Even though actual experiments to identify material properties are not performed on this work, analytical solution simulate actual experiments very well. To improve accuracy of the identification methods, sources of errors should be discussed. For DIC methods, displacement errors are evaluated by relative errors in L_2 -norm as in table 2. The causes of DIC displacement errors are from numerical errors such as truncation errors of optical flow, interpolation errors of bicubic spline and interpolation errors of Q4 shape functions. Quality of speckle images such as speckle patterns and speckle sizes can also affect DIC errors. In figure 15, the analytical displacements reflect the inherent errors that are in DIC displacements. The steep displacement gradients along x and y axis of the plate that are difficult to measure by optical flow DIC cause irregular distribution of DIC displacements. The DIC strains that are computed by DIC displacements in eq. (34) are dominated by numerical errors or noises. Some studies use analytical solutions to smooth out these noises known as integrated approach ⁽⁴⁾. For this study, the noisy DIC strains that can be also smoothed out by MNET are represented by FEM strains as in figure 16 (b), (d), and (f). The distribution of FEM strains in fig. 16 almost resembles the distribution of exact strains.

Not only DIC measurements but also MNET play an important role to identify material properties. A benefit of using compliance coefficients instead of Young's modulus and Poisson's ratio in MNET is to reduce computational terms of strain gradients in sensitivity matrix \mathbf{A} . However, this new method should be observed for identification errors because of little studies in the literatures. First, the noisy DIC strains can be the inputs for MNET to obtain material parameters. After that, the interconnection errors of DIC errors and MNET errors can be observed through the percentage errors of the Young's modulus, shear modulus and Poisson's ratio as in table 3 and 4. The interconnection errors of DIC errors and MNET errors are how MNET errors interact with DIC errors.

The errors in measurements can be divided into two categories that are systematic errors and random errors. The systematic errors are the average of many measurements that differs from the exact value. The percentage errors of the Young's modulus, shear modulus and Poisson's ratio as in table 3 and 4 can be considered as systematic errors of this simulation and the average values of the Young's modulus, shear modulus and Poisson's ratio are the accuracy of overall measurement systems. To improve accuracy, the systematic errors should be minimized. The proper selections of displacement shape functions, intensity interpolations and FEM models can reduce systematic errors.

The different speckle patterns and different speckle sizes for each simulation introduce random errors for DIC. The uncertainty of DIC errors influences the variation of identification material parameters which are measured by standard deviation in table 3 and 4. Since optimization algorithm and FEM models do not introduce variation in the results for this simulation, they would not affect the standard deviation of material parameters in table 3 and 4. Intuitively, minimizing random errors depends on selections of speckle patterns and sizes.

The interaction of DIC errors and MNET errors may affect Young's modulus in table 4. For example, the unsymmetrical values of affect percentage errors of Young's modulus E_x and E_y in table 4 may have influences from relative L_2 -norm

errors of FEM model errors in section 2.4 and DIC errors in table 2. The DIC displacement error in y-direction (V) is more than the DIC displacement error in x-direction (U). The FEM displacement error in y-direction (V) is more than the FEM displacement error in x-direction (U). The Young's modulus error in y-direction (E_y) is more than The Young's modulus error in x-direction (E_x). Before using DIC and FEM model to study orthotropic material properties, the unsymmetrical errors of x-direction errors and y-direction errors should be minimized for better accuracy. The Young's modulus E_x should equal to E_y .

The limitation of computer simulation is how to apply the results from computer simulation into actual experiments. The speckle patterns and sizes should be controlled the same as speckle images in simulation. The camera noises and lighting noises that do not consider in simulation affect the experimental results. To optimize the methods, parameters of DIC and MNET should be examined both in experiments and in simulation.

3. Optical flow and discontinuous finite element formulation

Before measuring displacements by DIC, 1-D image intensity are created from eq.(12) with $u_0 = -1$ for node 1 to 6 and $u_0 = 1$ for node 7 to 11. The size of the speckle granule (R) is equal to 6 and the total number of speckle granule (s) is equal to 500 with 103 pixel for image sizes. Figure 17 shows measured displacements of two objects that are moved apart from each other as in figure 11. The measured displacements from optical flow based on continuous finite element formulation (U-FEM) have small errors in the node number 1 to node number 5 and the node number 7 to 11. Likewise, the measured displacements from optical flow based on discontinuous finite element formulation (U-DFEM) have small errors in the same node number as continuous finite element method. However, while there is the separation of two objects at the middle (node number 6 and 7), U-DFEM displacement is more close to U-Exact than U-FEM.

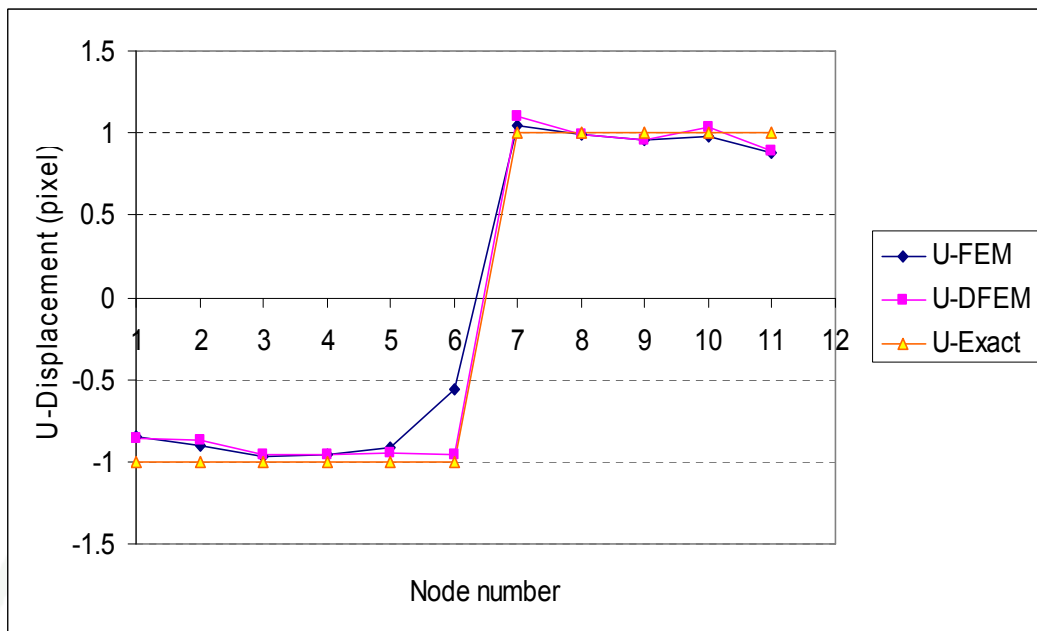


Figure 17 Measured displacements of optical flow based on continuous finite element (U-FEM), discontinuous finite element (U-DFEM) compared with exact displacement (U-Exact).

In figure 18, first absolute error (error of U-FEM) is computed from exact displacement (U-Exact) and continuous finite element (U-FEM). Other absolute error (error of U-DFEM) is computed from exact displacement (U-Exact) and discontinuous finite element (U-DFEM). The absolute errors define as

$$Error = |U_{exact} - U_{DIC}| \quad (52)$$

where U_{exact} is exact displacement (U-Exact) in figure 7 and U_{DIC} can be displacements from continuous finite element (U-FEM) or displacements from discontinuous finite element (U-DFEM). The absolute errors of U-DFEM of node number 5 and 6 are small than U-FEM. Even through other absolute errors of U-DFEM at other nodes are higher than U-FEM, they are in acceptable accuracy. However, the accuracy of both methods, FEM and DFEM, depends on speckle patterns. If different speckle patterns are created, accuracy might be different.

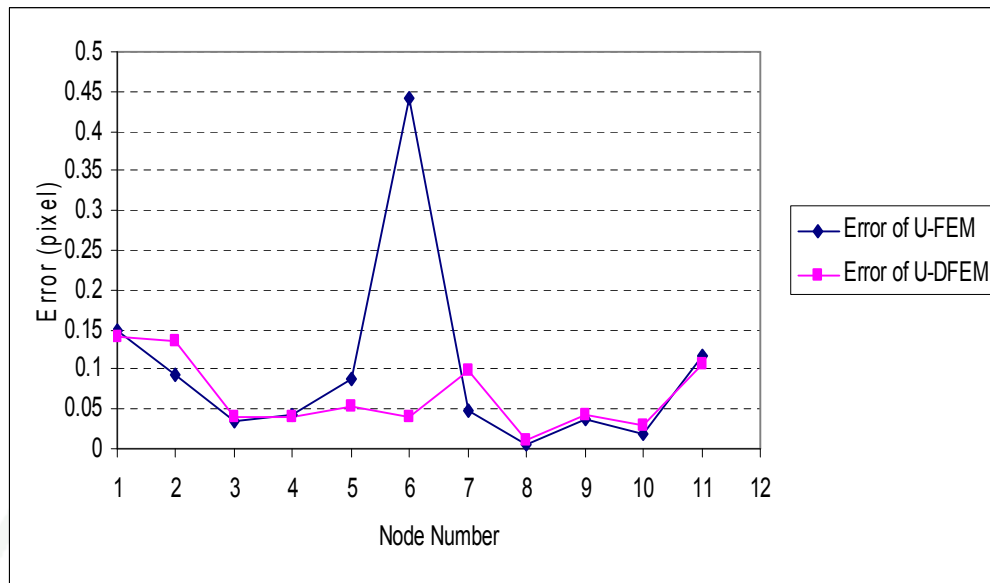


Figure 18 Absolute displacement errors of optical flow based on continuous finite element (Error of U-FEM), discontinuous finite element (Error of U-DFEM).

CONCLUSIONS AND RECOMMENDATIONS

1. Study of DIC algorithms

From the rigid body motion tests using synthetic images and imposed displacements, simple search methods in section 1.1 face difficulty to detect displacements that is less than one pixels because correlation coefficients are calculated at the pixel. This can be concluded that accuracy of the simple search algorithms is pixel accuracy. To capture displacements less than one pixel, subpixel algorithms such as N-R algorithms should be useful with minimum errors comparing to the simple search algorithms.

Next, using simple search methods and the cantilever beam to demonstrate DIC measurements can ensure the measurement accuracy. The DIC displacements compared with analytical solutions have a good agreements and acceptable accuracy. However, the lower accuracy in Z direction causes from small displacements that are difficult to measure by simple search methods. To increase accuracy, sub-pixel algorithms and high magnification of lens should be employed for DIC measurements.

2. Numerical experiments to identify elastic properties of materials

The computer simulation has been demonstrated to determined elastic parameters of materials using DIC and MNET algorithms. The optical flow DIC based on bicubic spline and Q4 shape function is developed and MNET is modified by using compliance coefficients. Then, the analytical solution of a plate with central hole helps to study DIC errors and MNET errors during development phases. The accuracy and precision of identification of material parameters can be approximated by systematic errors and random errors.

In this study, it has been shown that noisy DIC strains can be smoothed out by MNET algorithms. The results of smoothing noisy DIC strains by MNET are FEM

strains and elastic properties of materials. The percentage errors of identified elastic parameters infer the interconnection errors of DIC errors and MNET errors and systematic errors. The standard deviations of identified elastic parameters which have influences from DIC infer random errors.

The relative errors in L_2 -norm measure magnitude of DIC displacement errors in x and y direction. The relative errors in L_2 -norm of x-y displacement errors show asymmetry of DIC errors and FEM model errors that imply asymmetry of Young's modulus errors in orthotropic models. The causes of DIC displacement errors are from DIC numerical errors and quality of speckle patterns. This result should be studied for more details in future research.

The steep displacement gradients along x and y axis of the plate that cause irregular distribution of DIC displacements are difficult to measure by optical flow DIC. To improve accuracy of DIC measurements, high order of displacement shape function might be suitable to capture these steep displacement gradients.

3. Optical flow and discontinuous finite element formulation

The accuracy of optical flow based on DFEM formulation have better results at discontinuity of two objects than FEM formulation. However, If different speckle patterns are created, accuracy might be different. The accuracy depends on speckle size and patterns. If there are some numerical approximation errors in case of small subset sizes, DFEM trends to have more oscillation of results than FEM. For higher subset size, DFEM trends to have less oscillation of results than FEM.

LITERATURE CITED

- Akin, J.E. 2005. **Finite Element Analysis with Error Estimators: An Introduction to the FEM and Adaptive Error Analysis for Engineering Students**. Elsevier Science, Great Britain.
- Avril, S., M. Bonnet, A.-S. Bretelle, M. Grédiac, F. Hild, P. Jenny, F. Latourte, D. Lemosse, S. Pagano, E. Pagnacco and F. Pierron. 2008. Overview of identification methods of mechanical parameters based on full-field measurements. **Experimental Mechanics** 48 (4): 381-402.
- Babuška, I. and J.M. Melenk. 1997. The partition of unity method. **International Journal for Numerical Methods in Engineering** 40 (4): 727-758.
- Barber, J.R. 2002. **Elasticity**. 2nd Edition. Kluwer Academic Publishers, Netherlands.
- Besnard, G., F. Hild and S. Roux. 2006. “Finite-Element” displacement fields analysis from digital images: application to Portevin–Le Châtelier bands. **Experimental Mechanics** 46 (6): 789-803.
- Bing, P., X. Hui-min, X. Bo-qin and D. Fu-long. 2006. Performance of sub-pixel registration algorithms in digital image correlation. **Meas. Sci. Technol.** 17 (6): 1615-1621.
- Björck, Å. 1996. **Numerical Methods for Least Square Problems**. Society for Industrial and Applied Mathematics. North-Holland, Amsterdam.
- Bornert, M., F. Brémand, P. Doumalin, J.C. Dupré, M. Fazzini, M. Grédiac, F. Hild, S. Mistou, J. Molimard, J.J. Orteu, L. Robert, Y. Surré, P. Vacher and B. Wattrisse. 2009. Assessment of digital image correlation measurement errors: methodology and results. **Experimental Mechanics** 49 (3): 353-370.
- Bruck, H.A., S.R. McNeill, M.A. Sutton and W.H. Peters, III. 1989. Digital image correlation using Newton-Raphson method of partial differential correction. **Experimental Mechanics** 29 (3): 261-267.
- Burman, E., A. Quarteroni and B. Stamm. 2010. Interior penalty continuous and discontinuous finite element approximations of hyperbolic equations. **J. Sci. Comput.** 43 (3): 293-312.
- Burnett, D.S. 1987. **Finite Element Analysis: From Concepts to Applications**. Addison-Wesley.

- Cardon, A.H., H. Sol, W.P. Wilde, J. Visscher, K. Hoes and D. Dinescu. 2004. Mixed numerical-experimental techniques: past, present and future, pp. 551-560. *In* E. Gdoutos, eds. **Recent Advances in Experimental Mechanics**. Springer Netherlands.
- Cofaru, C., W. Philips and W.V. Paepegem. 2010a. Evaluation of digital image correlation techniques using realistic ground truth speckle images. **Meas. Sci. Technol.** 21 (5): 1-7.
- Cofaru, C., W. Philips and W. Van Paepegem. 2010b. Improved Newton-Raphson digital image correlation method for full-field displacement and strain calculation. **Optical Society of America** 49 (33): 6472-6484.
- Dally, J.W.A. and W.F.A. Riley. 1991. **Experimental Stress Analysis**. McGraw-Hill, Singapore.
- Doyle, J.F. 2004. **Modern Experimental Stress Analysis: Completing the Solution of Partially Specified Problems**. John Wiley & Sons, England.
- Epshteyn, Y., T. Khan and B. Rivière. 2009. Numerical solution of a one-dimensional inverse problem by the discontinuous galerkin method. **Mathematic and Computer Simulation** 79 (7): 1989-2000.
- Fries, T.-P. and T. Belytschko. 2006. The intrinsic XFEM: a method for arbitrary discontinuities without additional unknowns. **International Journal for Numerical Methods in Engineering** 68 (13): 1358-1385.
- Frocht, M.M. 1941. **Photoelasticity Volume I**. J. Wiley, U.S.A.
- Frocht, M.M. 1948. **Photoelasticity Volume II**. J. Wiley, U.S.A.
- Gibson, J.J. 1950. **The Perception of the Visual World**. Houghton Mifflin, Oxford, England.
- Gracie, R., H. Wang and T. Belytschko. 2008. Blending in the extended finite element method by discontinuous galerkin and assumed strain methods. **International Journal for Numerical Methods in Engineering** 74 (11): 1645-1669.
- Grédiac, M., E. Toussaint and F. Pierron. 2002a. Special virtual fields for the direct determination of material parameters with the virtual fields method 1 - principle and definition. **International Journal of Solids and Structures** 39 (10): 2691-2705.

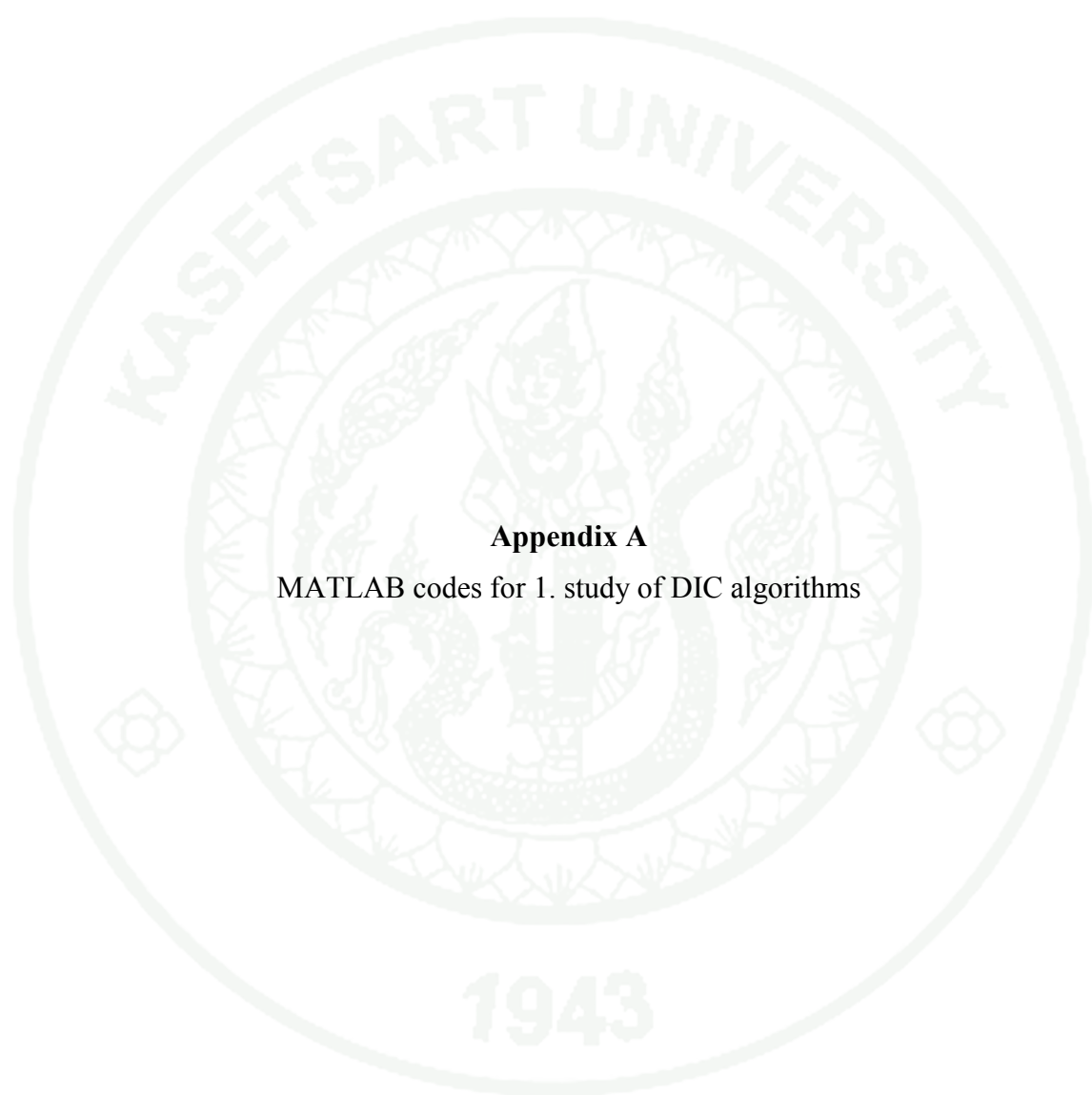
- Grédiac, M., E. Toussaint and F. Pierron. 2002b. Special virtual fields for the direct determination of material parameters with the virtual fields method 2 - application to in-plane properties. **International Journal of Solids and Structures** 39 (10): 2707-2730.
- Grédiac, M., E. Toussaint and F. Pierron. 2003. Special virtual fields for the direct determination of material parameters with the virtual fields method 3 - application to the bending rigidities of anisotropic plates. **International Journal of Solids and Structures** 40 (10): 2401-2419.
- Haddadi, H. and S. Belhabib. 2008. Use of rigid-body motion for the investigation and estimation of the measurement errors related to digital image correlation technique. **Optics and Lasers in Engineering** 46 (2): 185-196.
- Hild, F. and S. Roux. 2006. Digital image correlation: from displacement measurement to identification of elastic properties – a review. **Strain** 42 (2): 69-80.
- Horn, B.K.P. and B.G. Schunck. 1981. Determining optical flow. **Artificial Intelligence** 17:185-203.
- Hung, P.-C. and A.S. Voloshin. 2003. In-Plane Strain Measurement by Digital Image Correlation. **J. of the Braz. Soc. of Mech. Sci. & Eng.** 25 (3): 215-221.
- Jacquot, J.M.F.P. and J.M. Fournier. 2000. **Interferometry in Speckle Light: Theory and Applications : Proceedings of the International Conference 25-28 September 2000, Lausanne, Switzerland.** Springer Verlag.
- Lancaster, P. and K. Salkauskas. 1986. **Curve and Surface Fitting: An Introduction.** Academic Press, Great Britain.
- Lauwagie, T., H. Sol, G. Roebben, W. Heylen, Y. Shi and O. Van der Biest. 2003. Mixed numerical–experimental identification of elastic properties of orthotropic metal plates. **NDT&E International** 36 (7): 487-495.
- Lecompte, D., H. Sol, J. Vantomme and A.M. Habraken. 2005. Identification of elastic orthotropic material parameters based on ESPI measurements. *In* **SEM Annual Conference & Exposition on Experimental and Applied Mechanics.**
- Lecompte, D., A. Smits, H. Sol, J. Vantomme and D. Van Hemelrijck. 2007. Mixed numerical–experimental technique for orthotropic parameter identification using biaxial tensile tests on cruciform specimens. **International Journal of Solids and Structures** 44 (5): 1643-1656.

- Lecompte, D., A. Smits, S. Bossuyt, H. Sol, J. Vantomme, D. Van Hemelrijck and A.M. Habraken. 2006. Quality assessment of speckle patterns for digital image correlation. **Optics and Lasers in Engineering** 44 (11): 1132-1145.
- Li, B.Q. 2010. **Discontinuous Finite Elements in Fluid Dynamics and Heat Transfer**. Springer.
- Liu, G.R. and X. Han. 2003. **Computational Inverse Techniques in Non Destructive Evaluation**. CRC PressINC.
- Lu, H. and P.D. Cary. 2000. Deformation measurements by digital image correlation: implementation of a second-order displacement gradient. **Experimental Mechanics** 40 (4): 393-400.
- Lucas, B.D. and T. Kanade. 1981. An Iterative Image Registration Technique with an Application to Stereo Vision, pp. 674-679. *In Proceedings of the 7th international joint conference on Artificial intelligence - Volume 2*. Morgan Kaufmann Publishers Inc., Vancouver, BC, Canada.
- Mohammadi, S. 2008. **Extended Finite Element Method: For Fracture Analysis of Structures**. Wiley.
- Pagnacco, E., D. Lemosse, F. Hild and F. Amiot. (2005) **Inverse Strategy from Displacement Field Measurement and Distributed Forces Using FEA**, HAL - CCSD - CNRS.
- Pan, B., K. Qian, H. Xie and A. Asundi. 2008. On errors of digital image correlation due to speckle patterns, pp. 1-7. *In ICEM 2008: International Conference on Experimental Mechanics -Volume 7375*. SPIE.
- Peters, W.H. and W.F. Ranson. 1982. Digital imaging techniques in experimental stress analysis. **Opt. Eng.** 21 (3): 427-431.
- Post, D., B. Han and P. Ifju. 1994. **High Sensitivity Moiré: Experimental Analysis for Mechanics and Materials**. Springer-Verlag GmbH.
- Reddy, J. 2005. **An Introduction to the Finite Element Method**. McGraw-Hill.
- Reed, W.H. and T.R. Hill. 1973. **Triangular Mesh Methods for the Neutron Transport Equation**.
- Réthoré, J., F. Hild and S. Roux. 2007. Shear band capturing using a multiscale extended digital image correlation technique. **Comput. Methods Appl. Mech. Engrg.** 196 (49-52): 5016-5030.

- Réthoré, J., F. Hild and S. Roux. 2008a. Extended digital image correlation with crack shape optimization. **International Journal for Numerical Methods in Engineering** 73 (2): 248-272.
- Réthoré, J., J.-P. Tinnes, S. Roux, J.-Y. Buffière and F. Hild. 2008b. Extended three-dimensional digital image correlation (X3D-DIC). **C. R. Mecanique** 336 (8): 643-649.
- Sadd, M.H. 2009. **Elasticity: Theory, Applications, and Numerics**. Academic Press.
- Schreier, H. and M. Sutton. 2002. Systematic errors in digital image correlation due to undermatched subset shape functions. **Experimental Mechanics** 42 (3): 303-310.
- Schreier, H.W., J.R. Braasch and M.A. Sutton. 2000. Systematic errors in digital image correlation caused by intensity interpolation. **Opt. Eng.** 39 (11): 2915-2921.
- Sinha, J.K. and M.I. Friswell. 2003. The Use of Model Updating for Reliable Finite Element Modelling and Fault Diagnosis of Structural Components Used in Nuclear Plants. **Nuclear Engineering and Design** 223 (1): 11-23.
- Sutton, M.A., J.J. Orteu and H. Schreier. 2009. **Image Correlation for Shape, Motion and Deformation Measurements: Basic Concepts, Theory and Applications**. Springer.
- Sutton, M.A., W.J. Wolters, W.H. Peters, W.F. Ranson and S.R. McNeill. 1983. Determination of displacements using an improved digital correlation method. **Image Vision Computing** 1 (3): 133-139.
- Timoshenko, S. and J.N. Goodier. 1969. **Theory of Elasticity**. McGraw-Hill.
- Vendroux, G., N. Schmidt and W.G. Knauss. 1998. Submicron Deformation Field Measurements: Part 3. Demonstration of Deformation Determinations. **Experimental Mechanics** 38 (3): 154-160.
- Vendroux, G. and W.G. Knauss. 1998a. Submicron Deformation Field Measurements: Part 2. Improved Digital Image Correlation. **Experimental Mechanics** 38 (2): 86-92.
- Vendroux, G. and W.G. Knauss. 1998b. Submicron Deformation Field Measurements: Part 1. Developing a Digital Scanning Tunneling Microscope. **Experimental Mechanics** 38 (1): 18-23.
- Zill, D. and W. Wright. 2011. **Multivariable Calculus**. Jones & Bartlett Learning.



APPENDICES



Appendix A

MATLAB codes for 1. study of DIC algorithms

The examples of MATLAB programs using in the first section of this dissertation, study of DIC algorithms, consists of three programs. First, a MATLAB script file (or M-file), **ranspec.m**, is written to generate speckle patterns using equation (12).

M-file name: ranspec.m

```

% M-file to generate random speckle pattern
close all
clear all
clc
s = 500;           % Number of speckle granule
R = 4;            % Size of the speckle granule
is = 250;         % Square image sizes (pixel × pixel)
I1=zeros(is,is);
I2=zeros(is,is);
uo=0;ux=0;uy=0;   % Displacements and their gradients in x-direction
vo=0;vx=0;vy=0;   % Displacements and their gradients in y-direction
%1.creat image
for k=1:1:s
I = randint(1,1,[0,255]); % Random peak intensity of each speckle granule
xk=randint(1,1,[1,is]); % Random x-position of circle centers in the images
yk=randint(1,1,[1,is]); % Random y-position of circle centers in the images
for x = 1:1:is
    for y = 1:1:is
        IU(y,x) = I*exp(-((x-xk)^2)/R^2-((y-yk)^2)/R^2);
        ID(y,x) = I*exp(-((x-xk-uo-ux*x-uy*y)^2)/R^2-((y-yk-vo-vx*x-vy*y)^2)/R^2);
    end
end

```

```

end
I1=I1+IU;           % Summation of undeformed image
I2=I2+ID;           % Summation of deformed image
end
save('undeform','I1')
save('deform','I2')

```

Second, a MATLAB script file (or M-file), **DIC.m**, is written to measured displacements using simple search methods.

M-file name: DIC.m

```

%Simple search methods for DIC measurement
clear all
close all
clc
% Acquire image from file
load undeform
load deform
tic
IU=I1;
ID=I2;
% Create subset-template at center of undeformed image
I=IU(1+191:101+191,1+191:101+191);
% Calculate normalized correlation
for n=1:1:540
    for m=1:1:380
        cd(m,n) = corr2(I,ID(m:(m+100),n:(n+100))); % Correlation
    end
end

```



```

end
[max_c,imax]=max(abs(cd(:)));
[x,y]=ind2sub(size(cd),imax(1));      %Determine x and y positions
uo=x-191;      % Calculating displacements in x-direction
vo=y-191;      % Calculating displacements in y-direction
toc

```

Finally, a MATLAB script file (or M-file), **NR.m**, is written to measured sub-pixel displacements using N-R algorithm.

M-file name: NR.m

```

% DIC Newton Raphson algorithm
clear all
clc
load undeform;      % Acquire undeformed image from a file
load spcoeff      % Acquire spline coefficients from a file
f=I1(2:22,2:22);
P1=0;P2=0;P3=0;P4=0;P5=0;P6=0;
P7=0;P8=0;P9=0;P10=0;P11=0;P12=0;      % Initial parameters
for m=1:1:10      % Number of iteration
y=0;x=0;e=1;l=2;
for j=1:1:21
    k=2;
    for i=1:1:21
dx=(x-11);
dy=(y-11);
xx=x+P1+P3*dx+P4*dy+(P7*dx^2)/2+(P8*dy^2)/2+P9*dx*dy;
yy=y+P2+P5*dx+P6*dy+(P10*dx^2)/2+(P11*dy^2)/2+P12*dx*dy;

```

```

s=[1,yy,yy^2,yy^3,xx,xx*yy,xx*yy^2,xx*yy^3,xx^2,xx^2*yy,xx^2*yy^2,xx^2*yy^3,
xx^3,xx^3*yy,xx^3*yy^2,xx^3*yy^3];
g(j,i)=s*b(:,e);
clear s;
agP1=[b(5,e), b(6,e), b(7,e), b(8,e), 2*b(9,e), 2*b(10,e), 2*b(11,e), 2*b(12,e),
3*b(13,e), 3*b(14,e), 3*b(15,e), 3*b(16,e)];
s=[1; yy; yy^2; yy^3; xx; xx*yy; xx*yy^2; xx*yy^3; xx^2; xx^2*yy; xx^2*yy^2;
xx^2*yy^3];
dgP1(j,i)=agP1*s; clear agP1 s;
agP2=[b(2,e), 2*b(3,e), 3*b(4,e), b(6,e), 2*b(7,e), 3*b(8,e), b(10,e), 2*b(11,e),
3*b(12,e), b(14,e), 2*b(15,e), 3*b(16,e)];
s=[1; yy; yy^2; xx; xx*yy; xx*yy^2; xx^2; xx^2*yy; xx^2*yy^2; xx^3; xx^3*yy;
xx^3*yy^2];
dgP2(j,i)=agP2*s;
clear agP2 s;
dgP3(j,i)=dgP1(j,i)*dx; dgP4(j,i)=dgP1(j,i)*dy;
dgP5(j,i)=dgP2(j,i)*dx; dgP6(j,i)=dgP2(j,i)*dy;
dgP7(j,i)=(dgP1(j,i)*dx^2)/2; dgP8(j,i)=(dgP1(j,i)*dy^2)/2;
dgP9(j,i)=dgP1(j,i)*dx*dy; dgP10(j,i)=(dgP2(j,i)*dx^2)/2;
dgP11(j,i)=(dgP2(j,i)*dy^2)/2; dgP12(j,i)=dgP2(j,i)*dx*dy;
x=x+1;
if (i==k)
    e=e+1;
    k=k+1;
end
end
    end
if (j==l)
    e=e+1;
    l=l+1;
else
    e=e-20;
end
end

```

```

y=y+1;
x=0;
end

```

% Find gradient of residual function in eq. (10)

```

dcP1=0; dcP2=0; dcP3=0; dcP4=0; dcP5=0; dcP6=0; dcP7=0; dcP8=0; dcP9=0;
dcP10=0; dcP11=0; dcP12=0;

```

```

for j=1:1:21

```

```

    for i=1:1:21

```

```

        dcP1=((f(j,i)-g(j,i))*dgP1(j,i))+dcP1;
        dcP2=((f(j,i)-g(j,i))*dgP2(j,i))+dcP2;
        dcP3=((f(j,i)-g(j,i))*dgP3(j,i))+dcP3;
        dcP4=((f(j,i)-g(j,i))*dgP4(j,i))+dcP4;
        dcP5=((f(j,i)-g(j,i))*dgP5(j,i))+dcP5;
        dcP6=((f(j,i)-g(j,i))*dgP6(j,i))+dcP6;
        dcP7=((f(j,i)-g(j,i))*dgP7(j,i))+dcP7;
        dcP8=((f(j,i)-g(j,i))*dgP8(j,i))+dcP8;
        dcP9=((f(j,i)-g(j,i))*dgP9(j,i))+dcP9;
        dcP10=((f(j,i)-g(j,i))*dgP10(j,i))+dcP10;
        dcP11=((f(j,i)-g(j,i))*dgP11(j,i))+dcP11;
        dcP12=((f(j,i)-g(j,i))*dgP12(j,i))+dcP12;

```

```

    end

```

```

end

```

```

dcP=[dcP1;dcP2;dcP3;dcP4;dcP5;dcP6;dcP7;dcP8;dcP9;dcP10;dcP11;dcP12];
clear dcP1 dcP2 dcP3 dcP4 dcP5 dcP6 dcP7 dcP8 dcP9 dcP10 dcP11 dcP12;

```

% Find Hessian matrix

```

ddcP=zeros(12,12);

```

```

for j=1:1:21

```

```

    for i=1:1:21

```

```

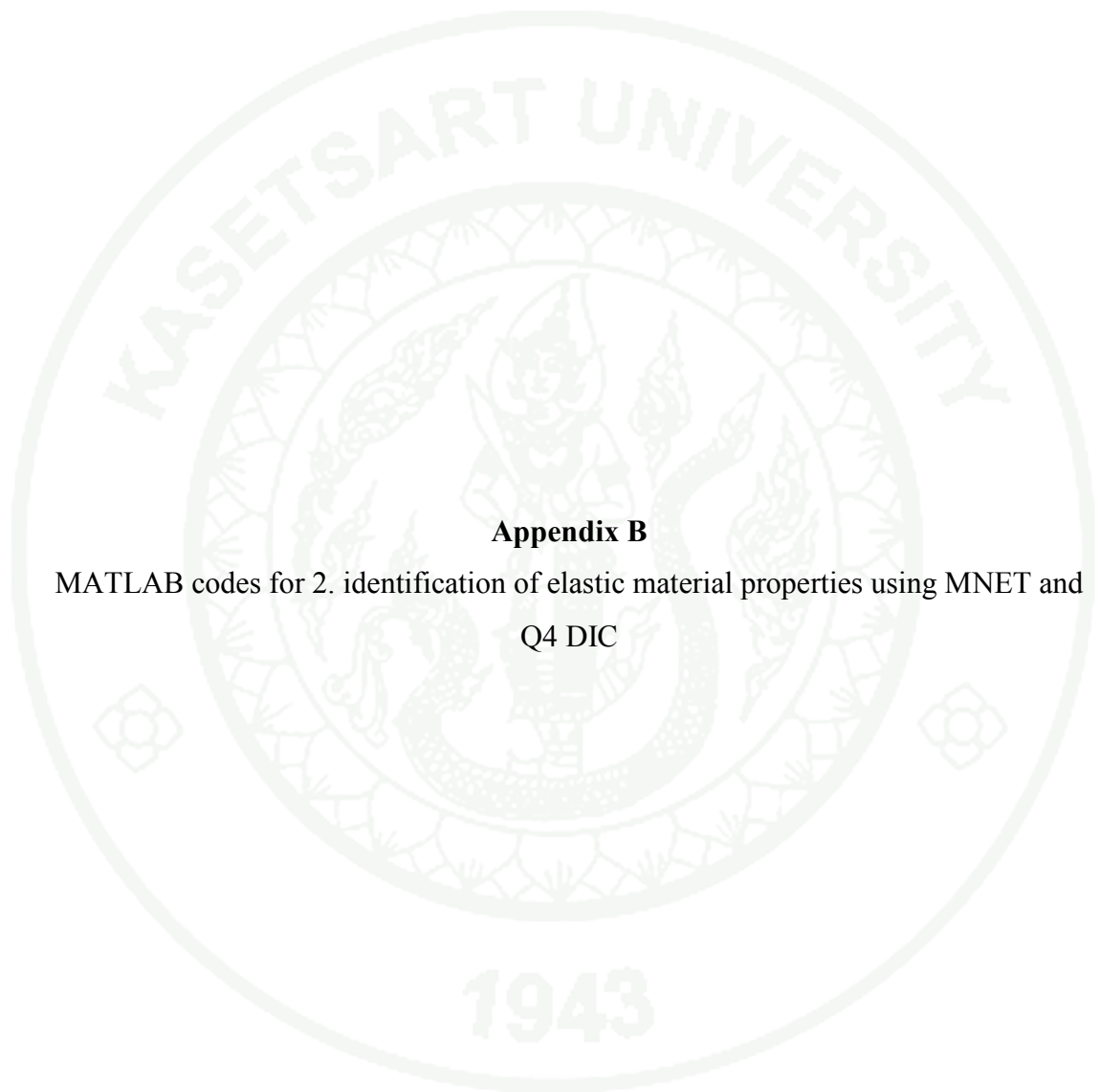
        dummy=[dgP1(j,i)*dgP1(j,i), dgP2(j,i)*dgP1(j,i), dgP3(j,i)*dgP1(j,i),
        dgP4(j,i)*dgP1(j,i), dgP5(j,i)*dgP1(j,i), dgP6(j,i)*dgP1(j,i), dgP7(j,i)*dgP1(j,i),

```

```

dgP8(j,i)*dgP1(j,i), dgP9(j,i)*dgP1(j,i), dgP10(j,i)*dgP1(j,i), dgP11(j,i)*dgP1(j,i),
dgP12(j,i)*dgP1(j,i);
.
.
.
dgP1(j,i)*dgP12(j,i), dgP2(j,i)*dgP12(j,i), dgP3(j,i)*dgP12(j,i),
dgP4(j,i)*dgP12(j,i), dgP5(j,i)*dgP12(j,i), dgP6(j,i)*dgP12(j,i),
dgP7(j,i)*dgP12(j,i), dgP8(j,i)*dgP12(j,i), dgP9(j,i)*dgP12(j,i),
dgP10(j,i)*dgP12(j,i), dgP11(j,i)*dgP12(j,i), dgP12(j,i)*dgP12(j,i)];
    ddcP=ddcP+dummy ;
    end
end
dddcP=ddcP\dcP;           % Calculating displacements for each iteration
Pnew(:,m)=[P1;P2;P3;P4;P5;P6;P7;P8;P9;P10;P11;P12]+dddcP;
P1=Pnew(1,m);P2=Pnew(2,m);P3=Pnew(3,m);P4=Pnew(4,m);P5=Pnew(5,m);P6=Pn
ew(6,m);P7=Pnew(7,m);P8=Pnew(8,m);P9=Pnew(9,m);P10=Pnew(10,m);P11=Pnew
(11,m);P12=Pnew(12,m);           % Updating Displacements and their
gradients
end

```



Appendix B

MATLAB codes for 2. identification of elastic material properties using MNET and Q4 DIC

In this section, the numerical experiments to find material properties are initiated in computer simulations. A MATLAB script file (or M-file), **exact.m**, is written to generate displacements which are from analytical solution of a plate with a hole for each pixel position. The displacement values for each position are kept in MATLAB data file (or MAT-file), **displacement.mat**. Next, the speckle patterns are generated from **ranspec.m** using displacement values from **displacement.mat**. The 16 bits grey values of undeformed and deformed images are kept in MAT-file, **undeform.mat** and **deform.mat**. The **spline.m** reads grey value data from MAT-file to compute bicubic spline coefficients. Finally, **assemble.m** calculates displacements using the Q4-DIC algorithm. The u and v displacements are saved in **disnum.mat**.

M-file name: exact.m

```
% Generating displacements from exact solution
clear all
x=linspace(0.0023,0.01055,206);      % ZOI width on x-axis
y=linspace(0.00825,0,206);          % ZOI height on y-axis
mu=0.45;                             % Poisson's ratio
E=2.4*10^9;                           % Young's modulus (Pa)
a=0.002;                               % Radius of a central hole
T=2*10^6;                              % Traction Force
s=T;
for j=1:1:206
    for i=1:1:206
        r=sqrt(x(i)^2+y(j)^2);      % Transform radius in x-y coordinate to polar
coordinate
        theta=atan(y(j)/x(i));      % Transform angle in x-y coordinate to polar
coordinate
        angle(j,i)=theta;
```



```

ur(j,i)=(T*r*cos(2*theta)/(2*E))*((1+mu)+4*(a^2/r^2)-
(1+mu)*(a^4/r^4))+(T*r/(2*E))*((1-mu)+(1+mu)*(a^2/r^2));
ut(j,i)=(-T*r*sin(2*theta)/(2*E))*((1+mu)+(2*(1-mu)*(a^2/r^2))+(1+mu)*(a^4/r^4));
u(j,i)=ur(j,i)*cos(theta)-ut(j,i)*sin(theta);
v(j,i)=ur(j,i)*sin(theta)+ut(j,i)*cos(theta);
if(x(i)==0)
    u(j,i)=0;
end
if (r<=0.002)
    u(j,i)=0;
    v(j,i)=0;
end
end
end
save('displacement', 'u','v')    % Writing displacements (u and v) to a file

```

M-file name: ranspec.m

```

% Generate random speckle
clear all
clc
s = 3000;           % Number of speckle granule
R = 3;             % Size of the speckle granule
is = 206;          % Image size (pixel × pixel)
I1 = zeros(is,is); % Gray values of undeformed images
I2 = zeros(is,is); % Gray values of deformed images
load displacement  % Read displacement values from the file
u=24970*u;        % Changing displacement units to pixel using 24,970 metre per
pixel

```

```

v=24970*v; % Changing displacement units to pixel using 24,970 metre per
pixel
for k=1:1:s
    I = normrnd(8000,1000); % Random peak intensity of each speckle granule
    xk=randint(1,1,[1,is]); % Random x-position of circle centers in the
images
    yk=randint(1,1,[1,is]); % Random y-position of circle centers in the
images

for x = 1:1:is
    for y = 1:1:is
        IU(x,y) = I*exp(-((x-xk)^2)/R1^2-((y-yk)^2)/R2^2);
        ID(x,y) = I*exp(-((x-xk-u(x,y))^2)/R1^2-((y-yk-v(x,y))^2)/R2^2);
    end
end
I1=I1+IU; % Summation undeformed image
I2=I2+ID; % Summation deformed image
end
save('undeform','I1')
save('deform','I2')

```

M-file name: spline.m

```

% Bicubic spline interpolation
load undeform
load deform
f=(I1(1:206,1:206));
g=(I2(1:206,1:206));
tic
% df/dx slope

```

```

e=1;
for i=1:204
    for j=1:204
        fx(i,j)=(f(i+e,j+1+e)-f(i+e,j-1+e))/2;
    end
end
end
% df/dy slope
e=1;
for i=1:204
    for j=1:204
        fy(i,j)=(f(i+1+e,j+e)-f(i-1+e,j+e))/2;
    end
end
end
% d2f/dxdy cross
e=1;
for i=1:204
    for j=1:204
        fxy(i,j)=((f(i+1+e,j+1+e)-f(i+1+e,j-1+e))-(f(i-1+e,j+1+e)-f(i-1+e,j-1+e)))/4;
    end
end
end
% Determine spline coefficient
i=1;j=1;s=203;e=1;
x1=-1/2;y1=-1/2;
x2=1/2;y2=-1/2;
x3=-1/2;y3=1/2;
x4=1/2;y4=1/2;
h=waitbar(0,'compute undeform spline f');
for m=1:41209
    C=[1,y1,y1^2,y1^3,x1,x1*y1,x1*y1^2,x1*y1^3,x1^2,x1^2*y1,x1^2*y1^2,x1^2*y1^
3,x1^3,x1^3*y1,x1^3*y1^2,x1^3*y1^3;
    .
    .

```

```

0,0,0,0,1,2*y4,3*y4^2,0,2*x4,4*x4*y4,6*x4*y4^2,0,3*x4^2,6*x4^2*y4,9*x4^2*y
4^2];
f1=[f(i+e,j+e);f(i+e,j+1+e);f(i+1+e,j+e);f(i+1+e,j+1+e);fx(i,j);fx(i,j+1);fx(i+1,j);fx(i+
1,j+1);fy(i,j);fy(i,j+1);fy(i+1,j);fy(i+1,j+1);fxy(i,j);fxy(i,j+1);fxy(i+1,j);fxy(i+1,j+1)];
a(:,m)=inv(C)*f1;
if(m==s)
    i=i+1;
    j=1;
    s=s+203;
else
    j=j+1;
end
waitbar(m/41209)
end
close(h)
clear fx fy fxy
%dg/dx slope
e=1;
for i=1:204
    for j=1:204
        gx(i,j)=(g(i+e,j+1+e)-g(i+e,j-1+e))/2;
    end
end
% dg/dy slope
for i=1:204
    for j=1:204
        gy(i,j)=(g(i+1+e,j+e)-g(i-1+e,j+e))/2;
    end
end
% d2g/dxdy cross

```

```

e=1;
for i=1:204
    for j=1:204
        gxy(i,j)=((g(i+1+e,j+1+e)-g(i+1+e,j-1+e))-(g(i-1+e,j+1+e)-g(i-1+e,j-1+e)))/4;
    end
end
end
% Determine spline coefficient
i=1;j=1;s=203;e=1;
x1=-1/2;y1=-1/2;
x2=1/2;y2=-1/2;
x3=-1/2;y3=1/2;
x4=1/2;y4=1/2;
h=waitbar(0,'compute deform spline g');
for m=1:41209
    C=[1,y1,y1^2,y1^3,x1,x1*y1,x1*y1^2,x1*y1^3,x1^2,x1^2*y1,x1^2*y1^2,x1^2*y1^
    3,x1^3,x1^3*y1,x1^3*y1^2,x1^3*y1^3;
    .
    .
    .
    0,0,0,0,1,2*y4,3*y4^2,0,2*x4,4*x4*y4,6*x4*y4^2,0,3*x4^2,6*x4^2*y4,9*x4^2*y
    4^2];
    g1=[g(i+e,j+e);g(i+e,j+1+e);g(i+1+e,j+e);g(i+1+e,j+1+e);gx(i,j);gx(i,j+1);gx(i+1,j);g
    x(i+1,j+1);gy(i,j);gy(i,j+1);gy(i+1,j);gy(i+1,j+1);gxy(i,j);gxy(i,j+1);gxy(i+1,j);gxy(i+
    1,j+1)];
    b(:,m)=inv(C)*g1;
    if(m==s)
        i=i+1;
        j=1;
        s=s+203;
    else
        j=j+1;

```

```

end
waitbar(m/41209)
end
close(h)
save ('spcoeff','a','b')
toc

```

M-file name: assemble.m

```

%Assembly stiffness matrix
clear all
clc
close all
load spcoeff
% Calculating stiffness matrix and force matrix of optical flow
h=waitbar(0,'calculating k & f');
tic
kk=zeros(8,8,841);
ff=zeros(8,1,841);
e=1;d=29;
for ii=1:841
x=0;
y=0;
sx=x+0.5;
sy=y+0.5;
for j=1:7
for i=1:7
kk(1:8,1:8,ii) = kk(1:8,1:8,ii) + k(a(:,e),sx,sy);
ff(1:8,1,ii) = ff(1:8,1,ii) + f(a(:,e),b(:,e),sx,sy);
x=i/7;

```



```

sx=x+0.5;
e=e+1;
    end
x=0;
sx=x+0.5;
y=j/7;
sy=y+0.5;
e=e+196;
    end
if(ii==d)
    e=e-196;
    d=d+29;
else
    e=e-1414;
    end
waitbar(ii/841)
end
close(h)
% Number node for each element
j=1;i=0;k=29;
for e=1:841
    t(1,j)=e+i;
    t(2,j)=e+1+i;
    t(3,j)=e+30+i;
    t(4,j)=e+31+i;
    j=j+1;
    if e==k
        i=i+1;
        k=k+29;
    end
end
end
% Stiffness matrix assembly

```

```

t=t';
kuv=sparse(1800,1800);
h=waitbar(0,'Assemble k');
for e=1:841
r=1;

for i=1:8
if(i==1|i==3|i==5|i==7)
c=1;
for j=1:8
if(j==1|j==3|j==5|j==7)
kuv((t(e,r)+(t(e,r)-1)),(t(e,c)+(t(e,c)-1)))=kuv((t(e,r)+(t(e,r)-1)),(t(e,c)+(t(e,c)-
1)))+kk(i,j,e);
end
if(j==2|j==4|j==6|j==8)
kuv((t(e,r)+(t(e,r)-1)),(t(e,c)+t(e,c)))=kuv((t(e,r)+(t(e,r)-
1)),(t(e,c)+t(e,c)))+kk(i,j,e);
c=c+1;
end
end
end
if(i==2|i==4|i==6|i==8)
c=1;
for j=1:8
if(j==1|j==3|j==5|j==7)
kuv((t(e,r)+t(e,r)),(t(e,c)+(t(e,c)-1)))=kuv((t(e,r)+t(e,r)),(t(e,c)+(t(e,c)-
1)))+kk(i,j,e);
end
if(j==2|j==4|j==6|j==8)
kuv((t(e,r)+t(e,r)),(t(e,c)+t(e,c)))=kuv((t(e,r)+t(e,r)),(t(e,c)+t(e,c)))+kk(i,j,e);
c=c+1;
end

```

```

    end
    r=r+1;
end
end
waitbar(e/841)
end
close(h)
% Force matrix assembly
fuv=sparse(1800,1);
h=waitbar(0,'Assemble f');
for e=1:841
    r=1;
    for i=1:8
        if(i==1|i==3|i==5|i==7)
            fuv((t(e,r)+(t(e,r)-1)),1)=fuv(t(e,r)+((t(e,r)-1)),1)+ff(i,1,e);
            r=r+1;
        end
    end
end
r=1;
for i=1:8
    if(i==2|i==4|i==6|i==8)
        fuv((t(e,r)+t(e,r)),1)=fuv((t(e,r)+t(e,r)),1)+ff(i,1,e);
        r=r+1;
    end
end
waitbar(e/841)
end
close(h)
% Displacement calculation
uv=kuv\fuv;
m=1;
for i=1:30

```

```

for j=1:30
    u(i,j)=uv(m);
    m=m+2;
end
end
m=2;
for i=1:30
    for j=1:30
        v(i,j)=uv(m);
        m=m+2;
    end
end
save('disnum','u','v')
toc

```

The triangular finite element mesh is created by partial differential equation toolbox (PDE-toolbox). The node positions, node numbers and element numbers are exported to **geo.mat** in p and t matrices. To determine selected elements on a square ZOI, **select.m** is written by using data from **geo.mat**. For selected procedures, three node positions of each element should be in ZOI after that element numbers can be identified. The selected element numbers are kept in **sel.mat**. The DIC displacements from quadrilateral elements are interpolated to each node of FEM triangular elements. Subsequently, strains at the centroid of triangular elements can be determined by differentiating displacement functions using **DICFEMdis.m**.

M-file name: select.m

```

% Selecting FEM elements on ZOI
clear all
clc

```



```

load disnum                % DIC displacement
load sel                    % Selected FEM element in ZOI
% Collecting position of triangle element node
[m,n]=size(e);
for i=1:n
    posx(1:3,i)=[p(t(e(1,i),1),1);p(t(e(1,i),2),1);p(t(e(1,i),3),1)];
    posy(1:3,i)=[p(t(e(1,i),1),2);p(t(e(1,i),2),2);p(t(e(1,i),3),2)];
end
% Interpolation of DIC-displacements to triangle element node
uu=-v/24970;
vv=-u/24970;
x=linspace(0.0023402,0.01051,30); %Zone 1
y=linspace(0.0082098,4.0244e-005,30); %zone 1
for ee=1:n
    for node=1:3
        m=1;
        for j=1:29
            n=1;
            for i=1:29
                if (posx(node,ee) >= x(i))&&(posx(node,ee)<=x(i+1))
                    if (posy(node,ee)>= y(j+1))&&(posy(node,ee)<=y(j))
                        u1=[uu(m,n);uu(m,n+1);uu(m+1,n);uu(m+1,n+1)];
                        v1=[vv(m,n);vv(m,n+1);vv(m+1,n);vv(m+1,n+1)];
                        b=[1,x(i),y(j),x(i)*y(j);
                            1,x(i+1),y(j),x(i+1)*y(j);
                            1,x(i),y(j+1),x(i)*y(j+1);
                            1,x(i+1),y(j+1),x(i+1)*y(j+1)];
                        a=inv(b)*u1;
                        c=inv(b)*v1;
                        ut(node,ee)=a(1)+a(2)*posx(node,ee)+a(3)*posy(node,ee)+a(4)*posx(node,ee)*posy(
node,ee);

```



```

vt(node,ee)=c(1)+c(2)*posx(node,ee)+c(3)*posy(node,ee)+c(4)*posx(node,ee)*posy(
node,ee);
    end
end
    n=n+1;
    end
m=m+1;
end
end
end
end
end
% DIC strain calculation of each element
clear a b c i j m n n node uu vv u v u1 v1 x y
[m,n]=size(e);
sta=zeros(3,n);
for ee=1:n
x=posx(:,ee);
y=posy(:,ee);
u=ut(:,ee);
v=vt(:,ee);
a=[1,x(1),y(1);
    1,x(2),y(2);
    1,x(3),y(3)];
area=det(a);
b1=y(2)-y(3);
b2=y(3)-y(1);
b3=y(1)-y(2);
c1=x(3)-x(2);
c2=x(1)-x(3);
c3=x(2)-x(1);
sta(1,ee)=(b1*u(1)+b2*u(2)+b3*u(3))/area;
sta(2,ee)=(c1*v(1)+c2*v(2)+c3*v(3))/area;
sta(3,ee)=(c1*u(1)+b1*v(1)+c2*u(2)+b2*v(2)+c3*u(3)+b3*v(3))/area;

```

```

end
[m,n]=size(e);
sx=zeros(1,2127);
sy=zeros(1,2127);
sxy=zeros(1,2127);
for i=1:1:n
sx(e(i))=sta(1,i);
sy(e(i))=sta(2,i);
sxy(e(i))=sta(3,i);
end
save('straindata','sx','sy','sxy')

```

The M-file, **main3iso.m**, is written for quantifying isotropic property of materials. In the first part of **main3iso.m**, MATLAB codes are written for finite element methods formulated in section 2.4. In the second part of **main3iso.m**, MATLAB codes are written for optimization in inverse methods formulated in section 2.5. Moreover, the M-file, **main3it.m**, is written for quantifying orthotropic property of materials in order to compare accuracy with **main3iso.m** and theory.

M-file name: main3iso.m

% Finding material parameters using FEM and MNET using isotropic parameters

```
clc
```

```
load geo
```

```
E=1*10^9;
```

```
G=E/2/(1+0.5);
```

```
v=0.5;
```

```
c11=E/(1-2*v);
```

```
c22=c11;
```

```
c66=G;
```

```
% Node positions and element information
```

```
% Initial Young's modulus
```

```
% Initial shear modulus
```

```
% Poisson's ratio
```

```

c12=v12*c22;
D=[c11,c12,0;
   c12,c22,0;
   0,0,c66];
th=0.001;
ss=[1/E;-v/E;1/G];           % Compliance coefficients
clear E v G c11 c12 c22 c66;

er=[1;1;1];
er1=1;
i=1;
while (er1 > 0)              % Decision to stop iteration
kuv=assem(t,p,D,th);        % FEM stiffness calculation
[m,n]=size(t);
s=max(max(t));
s=s*2;
f=zeros(s,1);               % FEM Force matrix
f(3,1)=2.009685129;
f(33,1)=4.017766583;
f(35,1)=4.013549074;
f(37,1)=4.006240334;
f(39,1)=3.995083767;
f(41,1)=3.979731955;
f(43,1)=3.960717658;
f(45,1)=3.939895109;
f(47,1)=3.920513778;
f(49,1)=3.906575838;
f(5,1)=1.950740778;
% Boundary condition each node u & v = 0
b = [6  8   52  54  56  58  60  62  64  66  388  440
     466  512  514  522  594  758  874  876  880  1328
     1334 1336 1346 1720 1722 1724 19  67  69  71  73

```

```

75 77 79 81 83 389 407 411 467 595 597
753 755 871 881 1329 1331 1337 1727 1731 1733];

[h,g]=size(b);
kuv(b,:)=[];
kuv(:,b)=[];
f(b,:)=[];
% Solving systems of linear equation
d=kuv\f;
u=zeros(1116,1);
v=zeros(1116,1);
n=1;
% Rearrange displacement calculation into matrix for post-processing
for e1=1:2232
    if(e1==6| e1==8 | . . . |e1==1731 | e1==1733)
        d1(e1,:)=0;
    else
        d1(e1,:)=d(n,:);
        n=n+1;
    end
end
n=1;
for e1=1:1116
    u(e1,:)=d1(n,:);
    n=n+2;
end
n=2;
for e1=1:1116
    v(e1,:)=d1(n,:);
    n=n+2;
end
ste=stress(t,p,D,th,d1); % FEM stress calculation
sta=strain(t,p,th,d1); % FEM strain calculation

```

% Identification of constitutive parameters

load straindata

b=zeros(3,1);

A=zeros(3,3);

tx=ste(1,:);

ty=ste(2,:);

txy=ste(3,:);

load sel

[e1,e2]=size(e);

m=e;

% Calculating updated compliance coefficient in equation (32)

for j=1:e2

A(1,1)=tx(m(j))^2+ty(m(j))^2+A(1,1);

A(1,2)=2*tx(m(j))*ty(m(j))+A(1,2);

A(2,1)=2*tx(m(j))*ty(m(j))+A(2,1);

A(2,2)=tx(m(j))^2+ty(m(j))^2+A(2,2);

A(3,3)=txy(m(j))^2+A(3,3);

b(1,1)=(sx(m(j))-sta(1,m(j)))*tx(m(j))+(sy(m(j))-sta(2,m(j)))*ty(m(j))+b(1,1);

b(2,1)=(sx(m(j))-sta(1,m(j)))*ty(m(j))+(sy(m(j))-sta(2,m(j)))*tx(m(j))+b(2,1);

b(3,1)=(sxy(m(j))-sta(3,m(j)))*txy(m(j))+b(3,1);

end

sd=inv(A)*b;

ss=ss+sd;

er=100*[abs(sd(1)/ss(1));abs(sd(2)/ss(2));abs(sd(3)/ss(3))];

dd=[ss(1),ss(2),0;

ss(2),ss(1),0;

0,0,ss(3)];

D=inv(dd);

c11(i)=D(1,1);

c12(i)=D(1,2);

c22(i)=D(2,2);

c66(i)=D(3,3);

```

if (er(1)<0.01 && er(2)<0.01 && er(3)<0.01)
er1=-1;
end
i=i+1;
end

```

M-file name: main3it.m

% Finding material parameters using FEM and MNET using isotropic parameters

```

clc
load geo
E1=1*10^9;
E2=1*10^9;
%G=E1/2/(1+0.5);
G=1000*10^6;
v12=0.5;
v21=0.5;
c11=E1/(1-v12*v21);
c22=E2/(1-v12*v21);
c66=G;
c12=v12*c22;
D=[c11,c12,0;
   c12,c22,0;
   0,0,c66];
th=0.001;
ss=[1/E1;-v12/E2;1/E2;1/G];
clear E1 E2 v11 v12 G c11 c12 c22 c66;

er=[1;1;1;1];

```



```

er1=1;
i=1;
while (er1 > 0)
kuv=assem(t,p,D,th);    % FEM stiffness calculation
[m,n]=size(t);
s=max(max(t));
s=s*2;
f=zeros(s,1);          % FEM force matrix
f(3,1)=2.009685129;
f(33,1)=4.017766583;
f(35,1)=4.013549074;
f(37,1)=4.006240334;
f(39,1)=3.995083767;
f(41,1)=3.979731955;
f(43,1)=3.960717658;
f(45,1)=3.939895109;
f(47,1)=3.920513778;
f(49,1)=3.906575838;
f(5,1)=1.950740778;
b=[6   8   52   54   56   58   60   62   64   66   388  440
    466  512  514  522  594  758  874  876  880  1328
    1334 1336 1346 1720 1722 1724 19   67   69   71   73
    75   77   79   81   83   389  407  411  467  595  597
    753  755  871  881 1329 1331 1337 1727 1731 1733]; %
Boundary condition
[h,g]=size(b);
kuv(b,:)=[];
kuv(:,b)=[];
f(b,:)=[];
% Solving system linear eq.
d=kuv\f;
u=zeros(1116,1);

```

```

v=zeros(1116,1);
n=1;
for e1=1:2232    %node*2
    if(e1==6| e1==8 | . . . | e1==1731 | e1==1733)
        d1(e1,:)=0;
    else
        d1(e1,:)=d(n,:);
        n=n+1;
    end
end
n=1;
for e1=1:1116
    u(e1,:)=d1(n,:);
    n=n+2;
end
n=2;
for e1=1:1116
    v(e1,:)=d1(n,:);
    n=n+2;
end
ste=stress(t,p,D,th,d1); % FEM stress calculation
sta=strain(t,p,th,d1); % FEM strain calculation
% Identification of constitutive parameters
load straindata
b=zeros(4,1);
A=zeros(4,4);
tx=ste(1,:);
ty=ste(2,:);
txy=ste(3,:);
load sel
[e1,e2]=size(e);
m=e;

```

```

for j=1:e2
A(1,1)=tx(m(j))^2+A(1,1);
A(1,2)=tx(m(j))*ty(m(j))+A(1,2);
A(2,1)=(tx(m(j))*ty(m(j)))+A(2,1);
A(2,2)=(tx(m(j))^2+ty(m(j))^2)+A(2,2);
A(2,3)=(tx(m(j))*ty(m(j)))+A(2,3);
A(3,2)=(tx(m(j))*ty(m(j)))+A(3,2);
A(3,3)=ty(m(j))^2+A(3,3);
A(4,4)=txy(m(j))^2+A(4,4);
b(1,1)=(sx(m(j))-sta(1,m(j)))*tx(m(j))+b(1,1);
b(2,1)=(sx(m(j))-sta(1,m(j)))*ty(m(j))+(sy(m(j))-sta(2,m(j)))*tx(m(j))+b(2,1);
b(3,1)=(sy(m(j))-sta(2,m(j)))*ty(m(j))+b(3,1);
b(4,1)=(sxy(m(j))-sta(3,m(j)))*txy(m(j))+b(4,1);
end
sd=inv(A)*b;
ss=ss+sd;
er=100*[abs(sd(1)/ss(1));abs(sd(2)/ss(2));abs(sd(3)/ss(3));abs(sd(4)/ss(4))];
dd=[ss(1),ss(2),0;
    ss(2),ss(3),0;
    0,0,ss(4)];
D=inv(dd);
c11(i)=D(1,1);
c12(i)=D(1,2);
c22(i)=D(2,2);
c66(i)=D(3,3);
if (er(1)<0.01 && er(2)<0.01 && er(3)<0.01 && er(4)<0.01)
er1=-1;
end
i=i+1;
end

```

CURRICULUM VITAE**NAME** : Mr. Rittipol Chantararat**BIRTH DATE** : May 19, 1976**BIRTH PLACE** : Khonkean, Thailand

EDUCATION :	<u>YEAR</u>	<u>INSTITUTE</u>	<u>DEGREE/DIPLOMA</u>
	1999	Suranaree Univ. of Tech.	B.Eng.(Mechanical Eng.)
	2003	Loyola Marymount Univ.	M.S. (Mechanical Eng.)

POSITION/TITLE : ---**WORK PLACE** : ---**SCHOLARSHIP/AWARDS** : ---